2020

Piezospectroscopic Sensing Systems - Multi-Scale and In-Situ Sensing Technology for Structural Integrity

Remelisa Esteves
University of Central Florida

PIEZOSPECTROSCOPIC SENSING SYSTEMS - MULTI-SCALE AND IN-SITU SENSING TECHNOLOGY FOR STRUCTURAL INTEGRITY

by

REMELISA P. ESTEVES
B.S. Embry-Riddle Aeronautical University, 2016

A thesis submitted in partial fulfillment of the requirements
for the degree of Master of Science
in the Department of Mechanical and Aerospace Engineering
in the College of Engineering and Computer Science
at the University of Central Florida
Orlando, Florida

Spring Term
2020

Major Professor:
Seetha Raghavan

ABSTRACT

The aerospace industry relies on nondestructive evaluation (NDE) to ensure aircraft safety and will benefit from methods that allow for early damage detection. Photoluminescence piezospectroscopy (PS) has demonstrated stress and damage sensing of substrates when coupled with α-alumina nanoparticles in a polymer matrix applied as a sensor coating. Alpha phase alumina exhibits photoluminescent spectral emission lines (R-lines) that shift due to changes in the stress state of the alumina. The coatings' capability for sensing early subsurface damage suggests the potential for implementing stress sensing paint for integrity monitoring of aircraft structures. To achieve a viable stress sensing coating that can be applied as a paint, materials for optimal sensing and processing need to be tailored for aircraft applications. In addition, advances in optics technology for area measurement and faster data collection are needed. In this work, manufacturing of the sensing paint was achieved by introducing alumina nanoparticles into an aircraft grade topcoat using 3 different processing approaches and the paint with the best dispersion was identified using quantitative luminescence intensity results. To maintain the ease of application through spraying, dispersant was added to the paint. Tensile tests on composite and aluminum substrates resulted in spectral shifts with applied loading that reveal non-uniform and non-recoverable stresses within the paint. Scanning electron microscopy showed microcracks verifying that the sensing paint experienced damage during loading. R1 peaks shift as the paint was heated and cooled, indicating the possibility that the paint is sensitive to temperature changes. Future iterations of the sensing paint will focus on improvements

in polymer mechanical properties and homogeneity on application, particle-to-polymer bonding and enhanced adhesion. Area measurement was achieved through the development and calibration of a hyperspectral imaging system using a laser with wider aperture. The long-term goal is to establish a standardized paint-based PS coating and optics technology for structural integrity monitoring of aircraft structures.

"Be willing to be uncomfortable. Be comfortable being uncomfortable. It may get tough, but it's a small price to pay for living a dream." – Peter McWilliams

ACKNOWLEDGMENTS

I would like to thank my advisor and Thesis Chair, Dr. Seetha Raghavan, for her guidance and support throughout this project. Thank you to my collaborators at Boeing - Hong Tat, Dr. Joseph Schaefer, and Dr. Samuel Tucker - for their advice and mentorship. Special thanks goes to Dr. Tucker for hosting me during my internship at Boeing. Thank you to my collaborator, Dr. Bauke Heeg at Lumium, for his involvement in developing the photoluminescence hyperspectral imager. Thank you to my collaborator, Dr. Ambrose Taylor at Imperial College, for his involvement in sample manufacturing early on in my journey. Thank you to my colleagues at the University of Central Florida for any assistance they have provided on my project and for bringing their enthusiasm to the lab. Lastly, I would like to thank my family for their never-ending love and support. This work was supported by the National Science Foundation under Grant Nos. IIP 1701983 and CMMI 1130837 and the NSF DCL INTERN opportunity at Boeing, St. Louis.

TABLE OF CONTENTS

LIST OF FIGURES

LIST OF TABLES

CHAPTER 1
INTRODUCTION

1.1 Nondestructive Evaluation for Structural Integrity of Aircraft

Prior to release into the market and during service, it is imperative that aircraft structures are safe for use. The presence of defects within such structures are caused by either the manufacturing processes of parts or in-use damage [3]. They tend to be unseen by the naked eye, and, if not detected early on, can lead to catastrophic failure of the aircraft. The types of defects that form vary depending on the material and the type of stresses and damage that the material experiences. Metals are commonly used in aircraft, especially in the airframes. They are widely used due to being cost efficient and because of their ductility. However, they are susceptible to fatigue damage, corrosion, creep and crack growth [4]. Composites have become more prevalently used in aircraft structures over the years, having advantages such as high strength-to-weight ratio, capability of being molded into complex shapes, elimination of stress concentrations due to rivets and joints, and reduced assembly time. However, the load-carrying capacity of these materials can be reduced due to delaminations, disbonds, porosity, voids, matrix defects, and cracks. During the aircraft's flight cycle, both metal and composite parts are vulnerable to cyclic loading, which can cause them to weaken over time. Structural defects are detrimental to aircraft safety; thus, there is a need to be able to detect visually unnoticeable defects efficiently and as early as possible before failure. For this purpose, nondestructive evaluation (NDE) methods have been developed for industry and in-lab use. While there is a wide range of NDE methods, optical NDE, in particular, have garnered more attention due to having

high precision and sensitivity [5]. Piezospectroscopy (PS) is an optical method that is explored in this work due to its ability to sense stress and damage in substrates that are subjected to load. Literature search on current optical methods was done to determine how PS compares with those methods.

1.2 Current Optical, Nondestructive Evaluation Methods

There are various optical NDE methods that are currently used in industry, including digital image correlation (DIC), infrared thermography, and shearography [3, 5]. Some emerging optical NDE methods include stress and strain sensing via spectroscopy [6, 7, 8, 9, 10, 11], hyperspectral imaging [12, 13, 14], and optical transmission scanning [15, 16, 17]. The focus of this work is on a spectroscopy based method, and the measurements will be compared with DIC measurements.

1.2.1 Digital Image Correlation

DIC is a non-contact method that provides full-field displacements and strains by comparing digital images of the specimen surface in the un-deformed and deformed states, respectively, based on digital image processing and numerical computing [18]. DIC works for any material with a speckled coating applied onto its surface. When the speckle-coated material is subjected to loading, a high-resolution camera captures images of the displacement of the speckles at the

micron level. DIC is capable of detecting surface damage, and subsurface damage would need to extend to the surface. It is sensitive to substrate surface effects due to environmental conditions and complex geometry.

1.2.2 Strain and Stress Sensing using Spectroscopy

Spectroscopy involves the characterization of emitted spectra that result from changes in the energy state of an excited system. This concept as been employed in several NDE methods including near-infrared spectroscopy (NIRS) [19, 12], Terahertz spectroscopy [20, 21, 22] and Raman spectroscopy [6, 7, 8, 9, 10, 11]. In particular, Raman spectroscopy has been frequently utilized to characterize and understand the unique properties of carbon nanotubes (CNTs). CNTs have demonstrated potential for strain sensing for structural health monitoring and are currently under research and development for this purpose [23, 24, 25, 26, 27]. The electromagnetic properties of single walled nanotubes (SWNT) are controlled by both their size and chirality, which allows for variation in electronic effects for SWNT of the same diameter. Based on these parameters, SWNT can possess semiconductor properties as well as metallic properties [7]. Specifically, SWNT with metallic configurations exhibit significant resonance when excited within a narrow band of excitation laser energies, which produce Raman spectra of higher intensity and clarity [28]. When these high-resolution peaks are fitted, they allow for more significant analysis into the SWNT. By highlighting particularly distinct bands, the locations of these peaks can be efficiently tracked. If SWNT experience external loading under

laser-induced resonance, the resulting Raman spectra are observed to shift toward increasingly large wavenumber. While Raman spectroscopy is based on atomic vibrational domains [6], photoluminescence is based on the light emission of materials due to the absorption of photons [29]. The focus of this work is the photoluminescence spectral peaks of alumina, which are used for their stress sensitivity.

1.3 Background on Piezospectroscopy

1.3.1 Theory of Piezospectroscopy

Piezospectroscopy (PS) is a stress sensing method that makes use of photoluminescence (PL) spectroscopy of α-alumina, a naturally photoluminescent material due to the presence of chromium ion impurities. During laser excitation of the chromium ions within the α-alumina, the ions emit radiation that transitions from the ground state to the higher energy quartet states. Then a non-radiative transition occurs from the higher energy quartet states to the lowest energy excited state. The radiation at the $^2\mathrm{E}_g$ energy level returns to the ground level as an E and 2A energy state, which results in the doublet emissions called R-lines (Figure 1.1) [30, 31].

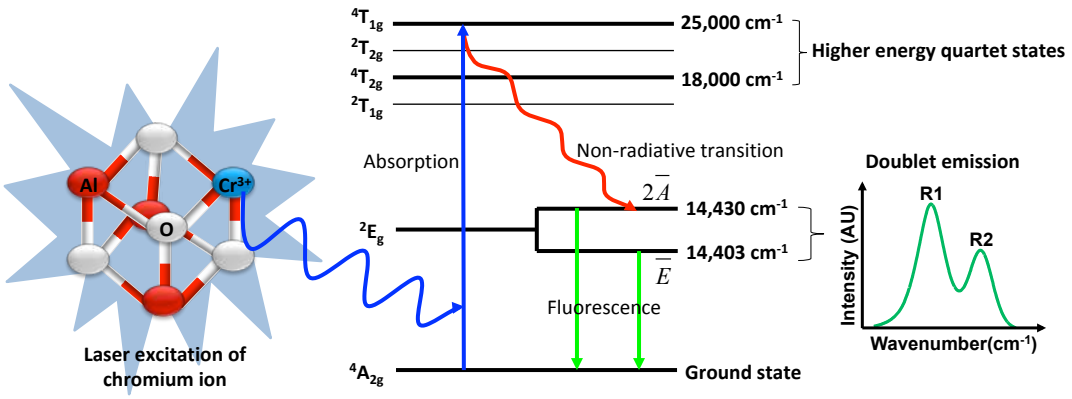

Figure 1.1: A schematic showing the emission of energy from chromium ions in α-alumina resulting in R-lines.

PS correlates the changes in the peak position of laser-induced spectral emission of photoluminescent materials when they are under stress. Historically, this method was applied to diamond-anvil pressure cells to visually observe pressure effects on materials using the R-line fluorescence in ruby [32]. It is also applicable to stress measurements of thermally grown oxide (TGO) layers in thermal barrier coatings (TBCs) in turbine engines [33, 34]. Through PS, the stress state of TBCs can be analyzed from the TGO, which is a chromium-doped α-alumina layer [35, 36]. The fundamental method is demonstrated when stress is applied to the material, where a shift in the R-lines can be observed. This phenomenon is known as the piezospectroscopic effect and can be expressed in the relationship shown in Equation 1.1 [37, 38]

$$\Delta\nu = \Pi_{ij}\sigma_{ij} \tag{1.1}$$

where Π_{ij} represents the effective piezospectroscopic coefficients, and $\Delta\nu$ represents the change in wavenumber from the peak shift while σ_{ij} is the stress tensor. Past work on PS on α-alumina [38] has shown that the peak shifts can be calibrated to stress for the α-alumina. He and Clarke [39] expanded on this work by relating the peak shifts to the first invariant of the stress tensor. Thus, present work on PS focuses on assessing stress on α-alumina nanoparticles embedded in a polymer matrix as a coating based on peak shifts.

1.3.2 Applications in Diamond-Anvil Cells

Diamond anvil cells (DACs) have been used in scientific experiments to study how materials behave under extreme environments. PS was used as a way to quantitatively measure pressure that is being applied to a material. Forman et al [40] worked with ruby, which is photoluminescent, to easily and accurately measure pressure based on R-line shifts. Eventually, the DAC was improved to include an optical fluorescence system, so that pressure can be measured rapidly [32]. Hirsch and Halzapfel [41] tested sapphire with DAC to study the effect of nonhydrostatic pressure on the Raman spectra of samples when they are subjected to pressures greater than 10 GPa. For these studies, photoluminescent materials were subjected to very high compressive stress (up to 30 GPa [32]) in order to capture significant R-line shifts. Studies that

apply PS to stress measurements in thermal barrier coatings (TBCs) have shown that R-line shifts can be captured in smaller ranges of applied stress.

1.3.3 Applications in Thermal Barrier Coatings

PS has been applied to structural integrity analysis of thermal barrier coatings (TBCs). TBCs protect turbine blades against high temperatures. When they fail, the underlying turbine blade is exposed, making it susceptible to thermal damage. Such damage can lead to costly down-times for repairs. Thus, there was a need to monitor damage progression in TBCs before they fail. The thermally grown oxide (TGO) layer that grows between the coating and bond coat has photoluminescent properties due to the presence of α-alumina. The photoluminescence signal coming from the α-alumina in TGO was used to determine the stress state of and assess damage on TBCs based on the spectral shifts induced by applied mechanical and thermal stress on the TGO [35, 42, 43]. These stresses were in the range of approximately 3-4 GPa [33]. PS of TGO layers have been used to measure oxidation [33] and residual stress [43] in TBCs. Sohn et al [42] have shown that average compressive stress in TGO was successfully captured with PS when the measured regions were not contaminated with engine deposits. Damage progression in TBCs were also assessed using PS and luminescence lifetime measurements of TGOs [35, 44].

1.4 Recent Work on Alumina Nanocomposites for Piezospectroscopy

It has been shown that the stress sensitivity for ruby, which consists of mineral corundum, is 2.56 and 2.65 cm^{-1}/GPa for R1 and R2 peaks, respectively, under uniaxial stress [39]. However, recent work has demonstrated that the sensitivity can be tailored by reducing bulk α-alumina into nanoparticulate form and distributing these particles within a polymer matrix to form a nanocomposite stress sensing material [37]. Stevenson et al performed calibration experiments to determine the relation between alumina particle content in epoxy matrix and sensitivity to stress as well as a method for characterizing dispersion in alumina-epoxy nanocomposites [45, 46]. This study eventually led to the development of PS coatings for stress sensing of substrates, which were studied by Freihofer et al [1, 47, 48, 49, 50]. Alumina particles were also embedded into carbon fiber reinforced polymer (CFRP) to improve the mechanical properties, specifically fracture toughness, while readily providing stress sensing capability [2, 51, 52, 53].

1.4.1 Volume Fraction Studies on Alumina Nanocomposites

Stevenson et al [45] performed compression tests on nanocomposite cuboids consisting of epoxy resin and varying volume fractions of α-alumina nanoparticles with 150 nm average particle size and 99.8 % purity. The nanocomposite cuboids were made and tested in accordance to ASTM D695 [54]. The peak shifts (or frequency shifts) were plotted with respect to

the applied compressive stress for each nanoparticle volume fraction tested, which showed a linear trend. The PS coefficient, which is an empirical value, was determined by taking the slope of the peak shift against the applied stress [38, 39]. It was found that the PS coefficient, which correlates with stress sensitivity, increases with increasing nanoparticle content for all of the volume fractions tested. Initial effort on characterizing the dispersion and volume fraction within alumina-epoxy nanocomposites was also done [46]. It was found that higher emission intensities correlated with increasing particle volume fraction and agglomerated areas, which could induce stress concentrations, within an alumina-epoxy nanocomposite. This finding demonstrated that the PS method can not only be used for stress sensing, but also for quality control of particle reinforced composites.

1.4.2 Piezospectroscopic Coatings for Stress and Damage Sensing

In Freihofer et al's [47] article, mechanics of particulate load transfer were investigated by comparing the experimental results from Stevenson et al's study [45] to theories by Eshelby [55] and Mori-Tanaka [56]. The load transfer theories that were explored in this work were shown to predict the stress in the particle for lower volume fractions of α-alumina. However, at higher loads, these theories underpredicted the particle stresses compared to the experimentally obtained results. The development of PS coatings started with an effort to create high adhesion through plasma spray coatings as a sensor material for structures [48]. However, the microstructure of plasma-spray coatings was shown upon loading to become inelastic and

anelastic. When substrates with the plasma spray-coating were subjected to load, the coating was sensing stress relaxation due to the behavior of the splat-like microstructure.

An alumina-epoxy based coating was developed as a stress-sensing coating. This PS coating configuration consisted of 20 vol% α-alumina nanoparticles with 150 nm average particle size and 99.8 % purity. In a study by Freihofer et al [1], the alumina-epoxy PS coating was tested on an open-hole tension (OHT) CFRP specimen, which was subjected to tensile load. DIC was used simultaneously during the load test to measure strain. It was found that the coating detected signs of internal ply damage at 76 % failure load well before DIC detected this damage at 92 % failure load (Figure 1.2). Although the PS coating had success in detecting subsurface damage before failure, it still needed to be configured to be applicable to aircraft structures.

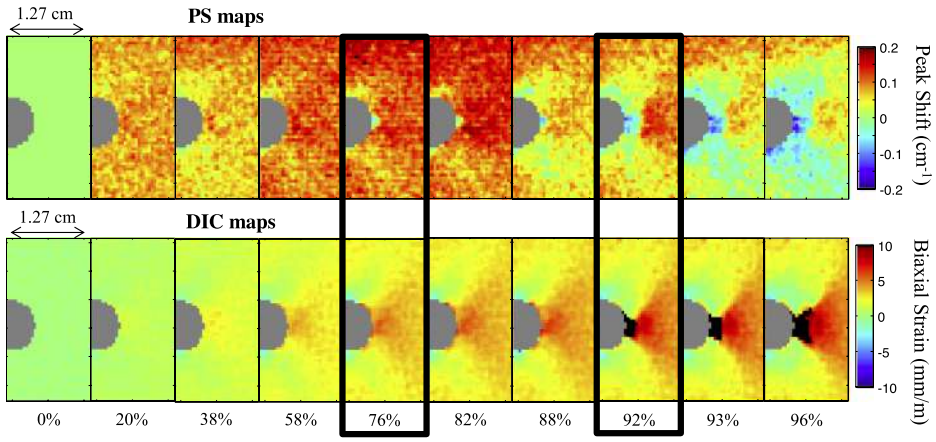

Figure 1.2: Tracking crack propagation and damage progression of OHT CFRP specimen with PS and DIC [1].

1.4.3 Exploration of Embedded Particles in Carbon Fiber Reinforced Polymers as Sensors

Hybrid carbon fiber composites (HCFRPs), where CFRPs are reinforced with particles for improved toughness, are heavily investigated as new structural materials [57, 58, 59]. These HCFRPs with varying alumina particle content were tested for dispersion and stress sensing capability [2, 60]. The concept of using these nanoparticles as sensors within CFRPs was explored by measuring their spectral shifts under load. While sensing capabilities were found to be limited because of particle-matrix debonding at the critical stress point, inspection of the dispersion of particles within the HCFRPs revealed non-uniform distribution of alumina for lower particle content, and more uniform distribution, but more agglomerations and sedimentation, of alumina for higher particle content (Figure 1.3) [2, 60]. This was achieved by using the intensity data collected from the alumina spectra.

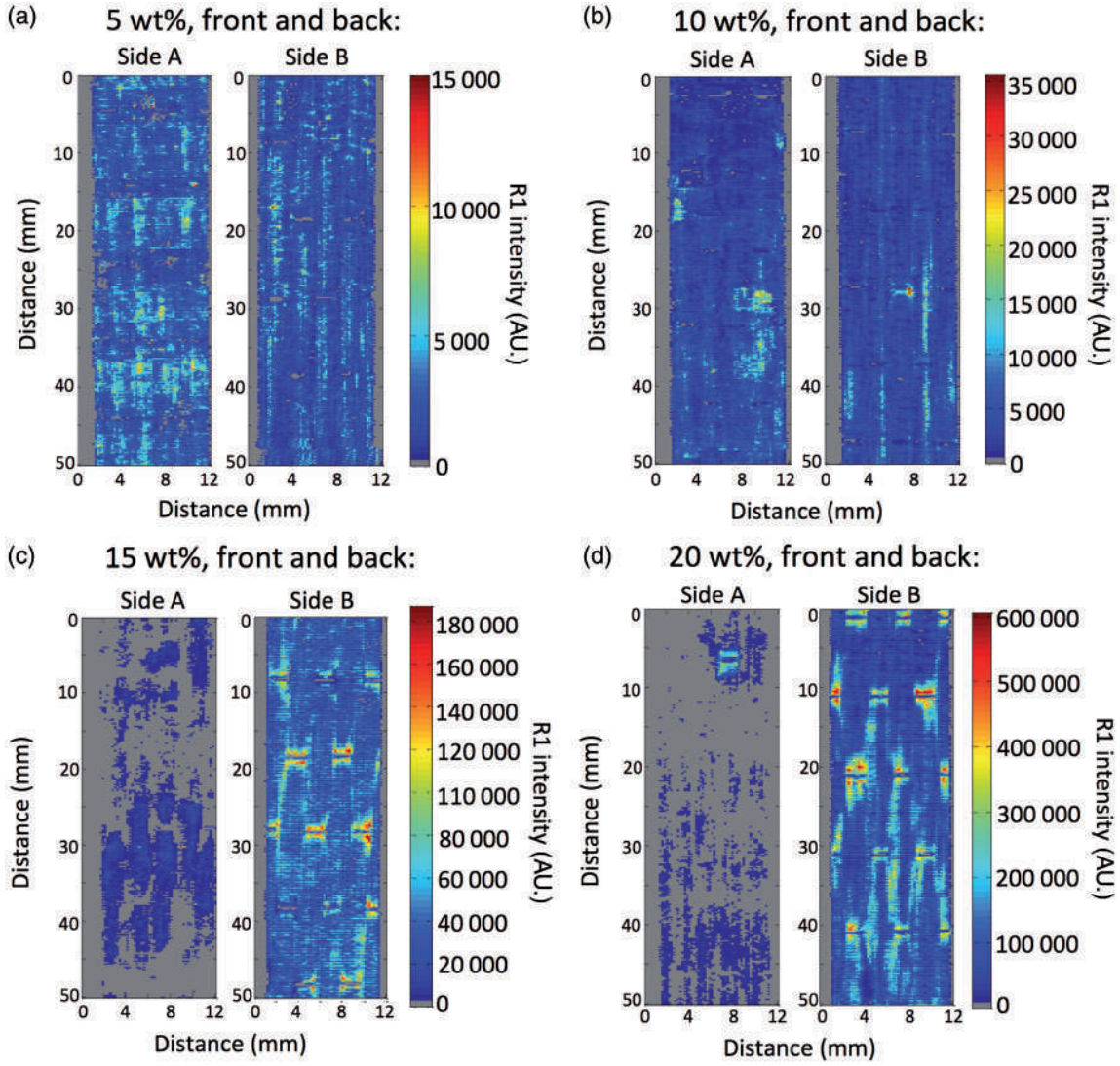

Figure 1.3: Intensity maps showing dispersion of alumina particles within HCFRPs of varying particle content [2].

The spectral results showed with high spatial resolution the location of agglomerates and provided insights on how to improve manufacturing. To address the issue with dispersion,

silane coupling agents (SCAs) were added into the HCFRPs [61]. It was found that the reactive SCA was more effective in improving the dispersion than the nonreactive SCA. The HCFRPs consisting of these SCAs were subjected to mechanical loading to test the HCFRPs' stress sensing capability [53]. Sensing was limited as the samples were subjected to tensile load because the particles had less load contribution than the carbon fibers. From this result, it was determined that the HCFRP configuration for sensor material is not ideal. However, photoluminescence intensities are useful for dispersion sensing.

1.5 Overview of Research

Although the current technology used to perform PS has demonstrated capability in sensing stress and damage, it still has limitations from a commercialization point of view. There is a lack of an optimized process to implement sensor material on aircraft structures, and data collection is time consuming with the prototype optics technology due to the point scanning that it offers. Improvements need to be made to the materials and optics technology to address these limitations. The sensor material needs to be configured as a paint-based PS coating that is suitable for aircraft structures while meeting the criteria for effective stress sensing. The optics technology needs to be able to take larger area scans and close-to real time data collection while ensuring mutli-scale spatial resolution and accurate stress resolution. In Chapter 2, the choices made on developing the material sensor configuration were justified based on validation analysis on the effect of particle volume fraction on stress sensing of composite and

metallic materials and criteria that the polymer matrix needed to meet. Chapter 3 discusses the different iterations of manufacturing the paint-based PS coating and the selection of processing approach based on particle dispersion and stress sensing. In Chapter 4, the selected coating processing approach was applied onto a notched metallic specimen and open-hole tension (OHT) CFRP specimen and analyzed for its stress sensing capability. The calibration of the photoluminescence hyperspectral imager (PHI), which was designed to be a scaled-up version of the prototype optics technology, is presented in Chapter 5. In Chapter 6, the conclusions of this study and future work is discussed.

CHAPTER 2
DEVELOPMENT OF MATERIAL SENSOR CONFIGURATION

2.1 Choice of Material Sensor

The selection of material sensor had to be considered for designing the paint-based PS coating. Previous work demonstrated successful stress-sensing with α-alumina nanoparticles (150 nm average particle size and 99.8 % purity) as material sensors in alumina-epoxy compression tests. Testing of different particle volume fractions in epoxy matrix was also done previously, as discussed in Chapter 1. Stevenson et al [45] have tested calibration compression samples with varying volume fractions. The findings show that the stress sensitivity can be numerically assessed through PS and increases with greater particle volume fractions. Freihofer et al [1] used a fixed volume fraction of particles (20 vol%) for tensile tests on alumina-epoxy PS coatings on an open-hole tension (OHT) CFRP sample based on the range of particle volume fractions tested by Stevenson et al [45], which showed that 25 vol% alumina in epoxy matrix provides sufficient sensitivity to stress while still achieving close-to uniform particle dispersion. This coating configuration was shown to successfully demonstrate stress sensing for soft laminates with a [45/-45/0/45/-45/90/45/-45/45/-45]$_S$ layup [1, 49].

Experiments were initiated to establish how volume fraction choices impact coating sensing performance. This chapter builds on these previous experiments to assess the appropriate volume fraction of alumina in coatings and the effect on sensing. In this work, an initial effort to answer the need to define optimal parameters for an ideal working configuration of

this PS coating was undertaken in order to enable the implementation of a technique to complement other NDE methods that are currently being used. Specifically, the volume fraction of α-alumina nanoparticles in these coatings for stress sensing was investigated in this study. This study also demonstrated how substrate type affects stress and damage sensing. Section 2.2 goes into detail on the differences in coating sensing on hard and soft laminate substrates. Additionally, up until now, no work was done to understand the capability of the alumina-epoxy PS coatings for metallic substrates. Thus, a mechanical test on aluminum tensile substrates with PS coatings with varying particle content was performed and analyzed, which is further discussed in Section 2.3.

2.2 Volume Fraction Effect on Piezospectroscopic Coatings on Hard and Soft Composite Laminates

Based on the experimental results of the calibration tests on different particle contents [45], it is expected that the alumina-epoxy PS coating's sensitivity to changes in stress, which correlates with the PS coefficient (Equation 1.1), increases as the particle volume fraction increases. However, the impact of volume fraction when applied as a coating and sensing response on various composite substrates (hard and soft laminates) were yet unknown. To study this further, the alumina-epoxy PS coatings tested were assessed for their stress sensitivity based on the signal-to-noise (SNR) and luminosity (rate of radiation emission based on R1 intensities per second), and the peak shift contour plots showing the qualitative stress distribution of the

loaded specimens. Here, spectral data from the three specimens with 5 vol% and 10 vol% volume fraction of α-alumina within a PS coating on hard laminate (with an elastic modulus 91 GPa) and 20 vol% volume fraction of α-alumina on soft laminate (with an elastic modulus of 38.6 GPa) were compared for their sensitivity in stress and damage detection. In addition, the damaged OHT CFRP test specimens from previous successful test [1] were assessed for post failure investigation.

The alumina-epoxy PS coatings were manufactured by Elantas PDG Inc. by mixing 150 nm α-alumina nanoparticles (Inframat Advanced Materials LLC) with 99.8 % purity in epoxy resin to achieve 5 vol%, 10 vol% and 20 vol% of particles. Each coating was applied onto an OHT CFRP substrate consisting of laminated IM7-8552 unidirectional tape. It is assumed that the thickness and stiffness of the coating are small and have a negligible effect on the substrate characteristics during loading. The laminates and corresponding coating configurations are shown in Table 2.1. The hard laminate specimens were loaded up to 88,964 N, while the soft laminate specimen was loaded up to 44,482 N. These were the maximum loads in which the specimens failed. PS data were collected using a 60 $\times$ 60 grid in a snake scan pattern, a measurement area of 25.4 mm^2, and a spatial resolution of 0.4 mm. The portable PS system collects data in a snake scan pattern by taking point scans of a defined area on the specimen with a laser probe. The system continues this pattern until it scans the entire defined area. To gain sufficient intensity with respect to the amount of particles in the coating, the maps for each PS coating were collected at various times. Table 2.1 shows the total collection time for each

PS coating. More information on the snake scan pattern and experimental setup are available in previous publications [1, 45].

After the specimens were loaded to failure, a map scan of each specimen was taken without applying load to assess the post failure residual stress. The PL data for each specimen was collected using a 200 $\times$ 200 grid in a snake scan pattern with an area of 40 mm^2 and a spatial resolution of 0.2 mm. The analysis of this data was conducted using a set of in-house, non-linear, least squares codes that allow for the processing of large data sets in a relatively short amount of processing time. This consists of a set of curve-fitting algorithms that process the unique R-line doublet that makes up the photo-luminescent response of α-alumina using two pseudo-Voigt functions. The details of curve fitting of experimental data using two pseudo-Voigt functions are further described in a previous publication [62].

To verify the signal response coming from the PS coatings, the representative R-lines for each coating configuration were analyzed, as shown in Figure 2.1. The experimental parameters and corresponding signal properties are shown in Table 2.1. The median SNRs were taken from the median of the spectra from one surface map, which consists of R-lines from 3600 point locations. The median coating luminosity was determined by taking the median intensity of one surface map divided by the collection time.

Table 2.1: Coating properties and experimental parameters for each PS coating

Laminate Type	PS Coating Volume Fraction	Collection Time per Point	Total Collection Time	Median Coating Luminosity	Median SNR
Hard	5 %	500 ms	32 minutes	8,529 counts/sec	42.85
Hard	10 %	200 ms	14 minutes	25,013 counts/sec	58.05
Soft	20 %	100 ms	8 minutes	104,698 counts/sec	94.27

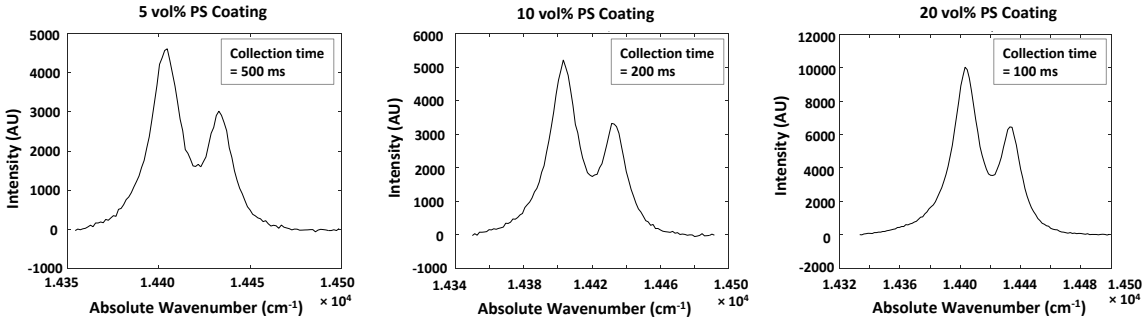

Figure 2.1: Representative R-lines for each PS coating with corresponding collection times. Laser power and beam diameter was kept consistent for each specimen.

The median SNRs measure the quality of the R-lines for each PS experimental parameter. The higher the median SNR and median coating luminosity, the lower the uncertainty in the peak position and the smoother the R-lines. It is shown that higher median SNR and median coating luminosity correlate with more distinctive peak shifts. With higher volume fractions of α-alumina nanoparticles in PS coating, higher median SNR and median luminosity can be obtained, which correlate with better signal quality. The differences in luminosity among the PS coatings tested are demonstrated in the dispersion maps as shown in Figure 2.2.

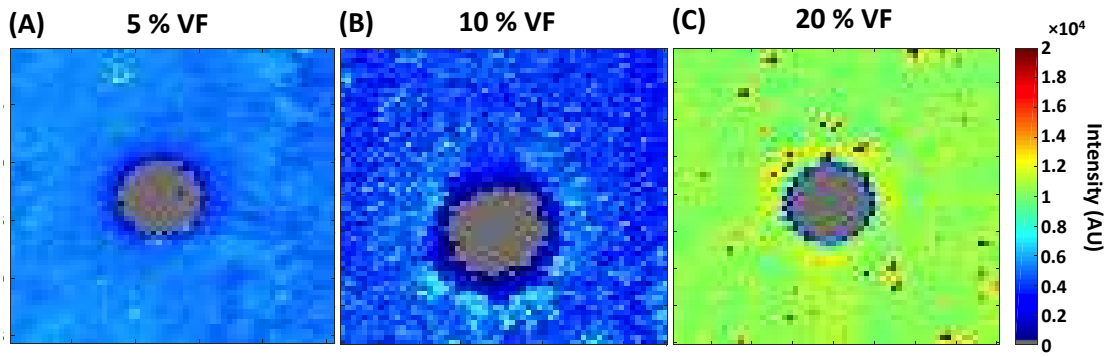

Figure 2.2: Contour maps showing α-alumina nanoparticle dispersion for (A) 5 %, (B) 10 % and (C) 20 % volume fraction PS coatings. Each map has dimensions of 25.4 mm $\times$ 25.4 mm. Also, note that "VF" is volume fraction.

The dispersion map for the 5 % volume fraction PS coating (Figure 2.2) showed that there was a small agglomerated spot at the top area. The dispersion map for the 10 % volume fraction PS coating showed that lowest presence of α-alumina nanoparticles and non-uniform disper-

sion around the hole of the OHT CFRP specimen. Although the dispersion map for the 10 % volume fraction PS coating suggests less uniformity in dispersion of α-alumina nanoparticles than the 5 % volume fraction PS coating, a fixed process was used to weigh the α-alumina nanoparticles to obtain the desired volume fraction for each coating. The non-uniformity in the presence of α-alumina nanoparticles in the 10 % volume fraction PS coating is most likely due to the application method of this coating, which may have led to a greater amount of agglomerations of nanoparticles. With the exception of a few agglomerated spots, the dispersion map for the 20 % volume fraction PS coating showed higher intensity readings in comparison to the dispersion maps for the 5 % and 10 % PS coatings.

The dispersion maps in Figure 2.2 further support that higher volume fractions of α-alumina correlate with higher SNR and luminosity. Thus, they correspond to higher intensities and lower uncertainty in the peak position. Although these dispersion maps indicate generally homogeneous dispersion, there were few areas in each PS coating with some variations in dispersion. It is expected that more agglomerations are present at higher volume fractions, which was clearly shown in the dispersion map for the 20 % volume fraction PS coating. However, these variations did not affect the PS coatings' capability in sensing changes in stress in the substrates.

Peak shift maps show shifts based on the type of stress that the specimens were experiencing. A positive shift indicates tensile stress, while a negative shift indicates compressive stress. Peak shift maps for the 5 % and 10 % volume fraction PS coatings were compared to observe differences in stress sensing capability on hard laminate as shown in Figure 2.3.

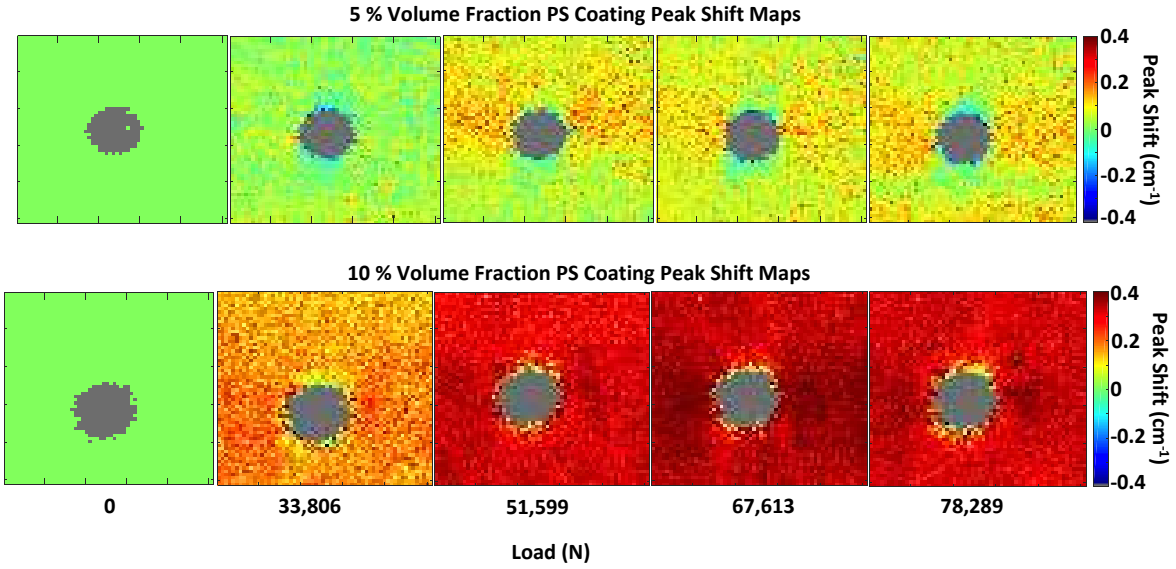

Figure 2.3: Stress sensing of two OHT CFRP specimens with 5 % and 10 % volume fraction PS coating with progressing loads. These specimens consist of composite substrates with hard laminate. Each map has dimensions of 25.4 mm $\times$ 25.4 mm.

Starting at 51,599 N, signs of tensile loading is clearly shown on the PS map for the 10 % volume fraction PS coating. At the same load, the PS map for the 5 % volume fraction PS coating showed only a slight change in stress. Based on this comparison, the 10 % volume fraction PS coating shows more sensitivity to changes in stress than the 5 % volume fraction PS coating. A higher PS coefficient for the 10 % volume fraction explains the higher stress sensitivity than the 5 % volume fraction PS coating [45]. The low SNR for the 5 % volume fraction PS coating may lead to ”noisier” peak shift maps due to the increased uncertainty of

the peak shift. The PS maps for both hard laminate specimens show strain release around the hole with increasing load. However, due to the high elastic modulus of this hard laminate substrate, there is not a significant change in the strain release compared to the soft laminate.

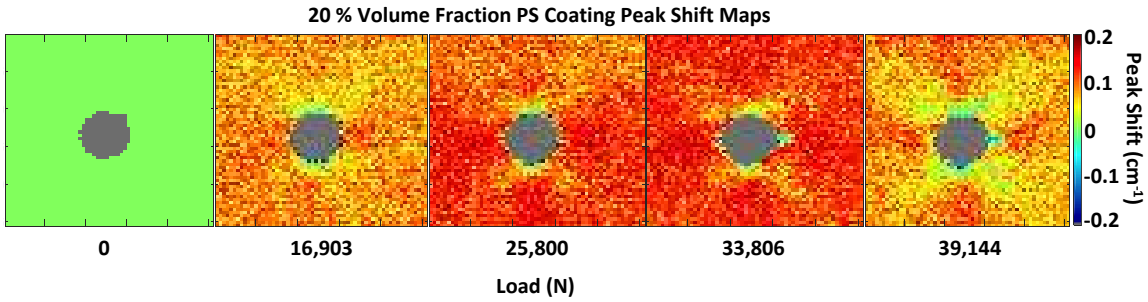

Figure 2.4: Stress sensing the OHT CFRP specimen 20 % volume fraction PS coating with progressing loads. This specimen consists of a composite substrate with soft laminate. Each map has dimensions of 25.4 mm $\times$ 25.4 mm.

The peak shift maps for the 20 % volume fraction PS coating were observed for the coating's stress sensing capability on soft laminate as shown in Figure 2.4. Intrinsic stress patterns are shown in the maps with progressive loading. Starting at 33,806 N, initiation of damage adjacent to the open-hole can be observed. This region was experiencing large tensile strains and was a likely location for the damage to initiate [1]. Work by Camanho [63] supports this phenomenon in which a simulation using continuum damage mechanics of a transversely isotropic open-hole tension composite specimen predicted initial fiber failure in the 0° ply in the same region. At 39,144 N, the PS map shows large stress gradients adjacent to the open

hole, which are likely caused by accumulating damage and redistribution of stresses [49]. Significant variation of stresses on the soft laminate is distinctly shown in the PS maps, which indicates that the PS coating can easily sense the changes in stress on this type of laminate. Specifically, more $\pm 45^{\circ}$ fibers in the soft laminate make it more susceptible to damage under uniaxial tensile load compared to the hard laminate. The reduction in stress localized near the hole is due to interlaminar damage in that area, which begins at around 76 % of the failure load. It is likely that higher stresses were redistributed throughout the larger area around the hole. As a result, these higher stresses over the larger area is less distinct, in terms of peak shift, than the localized reduction in stress near the hole. This phenomenon can be shown in previous work Freihofer et al [49]. The high SNR makes it easier to see the stress distributions across the sample surface due to less uncertainty in peak shifts. The high volume fraction also makes the nanocomposite PS coefficient higher. These combined effects made this sample the most optimal for demonstrating the sensing capability of PS coatings [1, 49].

Map scans of the OHT CFRP specimens with 5 %, 10 % and 20 % volume fraction of α-alumina were taken after failure. Figure 2.5 shows the post failure peak shift maps for the specimens. The peak shift map for each PS coating configuration in Figure 2.5 shows mostly uniform residual stress after substrate failure in the unloaded condition. The peak shift maps from Figures 2.3 and 2.4 indicate a changing stress state around the hole for all three specimens. The peak shift maps for the 5 % and 10 % volume fractions in the post failure condition indicate that the relaxed stress state at the fractured surface is retained, which indicates that cracking has occurred in the composite at this location. The peak shifts from the 20 % volume fraction PS

coating are not clear due to sustained larger deformations and more significant damage around the hole and the coating from the load tests in comparison with the hard laminate specimens.

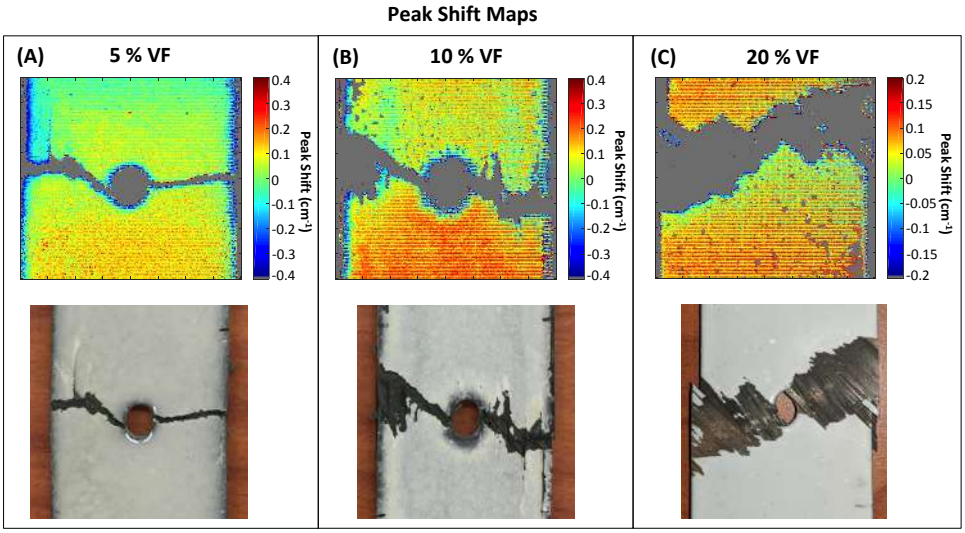

Figure 2.5: Contour maps with corresponding images of the OHT CFRP specimens showing peak shifts for (A) 5 %, (B) 10 % and (C) 20 % volume fraction PS coatings. Each map has dimensions of 40 mm $\times$ 40 mm. Also, note that "VF" is volume fraction.

This study demonstrated that the sensing capability of the PS coatings can be designed and tailored. Notable differences in capturing the stress variations that correlate with the presence of crack initiation and propagation in each OHT CFRP specimen were observed in the PS maps. For the hard laminates, the 10 % volume fraction PS coating showed more sensitivity than the 5 % volume fraction PS coating due to it having higher SNR. Comparing the PS maps

for the hard laminates and the soft laminate, the stress contours are more clearly observable for the PS coating on soft laminate with lower applied loads since it has more $\pm 45^{\circ}$ fibers than the hard laminate. The PS maps for the 20 % volume fraction PS coating show more features than the rest of the coatings due to it having the best median SNR and highest volume fraction of nanoparticles; and due to the soft laminate experiencing more progressive damage before failure than the hard laminate. A novel conclusion is that very significant qualitative differences observed between the hard and soft laminates suggest that the PS coatings can detect different failure modes that are specific to the substrates' laminate type. Other factors were considered when determining the necessary attributes for an effective PS coating. One factor is luminosity, which is independent of substrate type and is one of the attributes that makes the 20 % volume fraction PS coating more appealing. Another factor that was considered is the feasibility of manufacturing the coating and creating a homogeneous particle dispersion, which is being addressed in this work. Peak shifts indicating that relaxed stress state at the fractured surface was retained and more distinctive on the post failure peak shift maps for the 5 % and 10 % volume fraction PS coating than for the 20 % volume fraction PS coating. Future work will focus on investigating coating degradation under various environmental conditions and studying the different substrate laminate types with a consistent volume fraction. While visual inspection does not show any distinct sign of coating delamination in the areas where the fibers were still intact, further inspection of the coating can be done to determine whether damage was induced on it during and after load tests. Future efforts will relate the peak shifts to the substrate stress using multiscale modeling. To assess the effect of varying particle volume

fractions on stress sensitivity, the PS coefficients will be determined empirically with additional calibration experiments. These coefficients, along with the SNRs, will be used to determine the stress uncertainty to further evaluate particle volume fraction effectiveness.

Based on previous work on alumina-epoxy sensing materials and assessments made in this section, the particle volume fraction that was selected for paint-based PS coating was 20 vol%. The PS coating with this volume fraction of particles has demonstrated success in detecting damage initiation at the subsurface level prior to failure of the underlying composite substrate [1]. It is capable of showing more features of a composite substrate, which is useful for damage detection. It has the best SNR and intensity reading out of all the volume fractions tested. This ensures the least uncertainty in the R-line peak positions, which is needed for accurate peak shift measurements. This volume fraction has also shown high sensitivity to stress while maintaining close-to uniform dispersion and strong adhesion to the substrate. Thus far, the effect of volume fraction on PS coatings applied to composites has been demonstrated. In the next section, the effect of volume fraction on PS coatings applied to metallic substrates is discussed.

2.3 Volume Fraction Effect on Piezospectroscopic Coatings on Metallic Substrates

Motivated by the previous studies, the application of stress sensing coating is currently being investigated so that it can be extended to several materials and complex loading scenarios. This study is part of the study on the capability of the PS coating to detect stress concentration and

damage due to subsurface notch in a metallic substrate. Polymer nanocomposite coatings with 1 vol% and 10 vol% of α-alumina were applied to Al-2024 tensile specimens with a notch on the back of the substrate on which the coating is applied. The spectral data from the specimens under tensile load are compared for stress and damage sensing capability of the coatings.

Al-2024 tensile substrates were coated with PS coatings consisting of 1 vol% and 10 vol% α-alumina nanoparticles with an average particle size of 150 nm within an epoxy matrix. The substrates were machined and prepared in accordance with ASTM E8-04 [64]. In order to capture and monitor the development of the subsurface damage, a 0.25" $\times$ 0.16" $\times$ 0.08" notch was introduced in both substrates on the face opposite of the surface where the coatings had been applied.

Figure 2.6 shows the experimental setup for data collection to investigate stress sensing on an aluminum sample using the PS method. A servohydraulic MTS universal testing machine was used to apply uniaxial tensile load to the samples until failure load was reached. A crosshead displacement rate of 1 mm/min was used for the displacement controlled tensile tests. PL scans of the coatings were conducted at every 4 kN increment while the load was held constant.

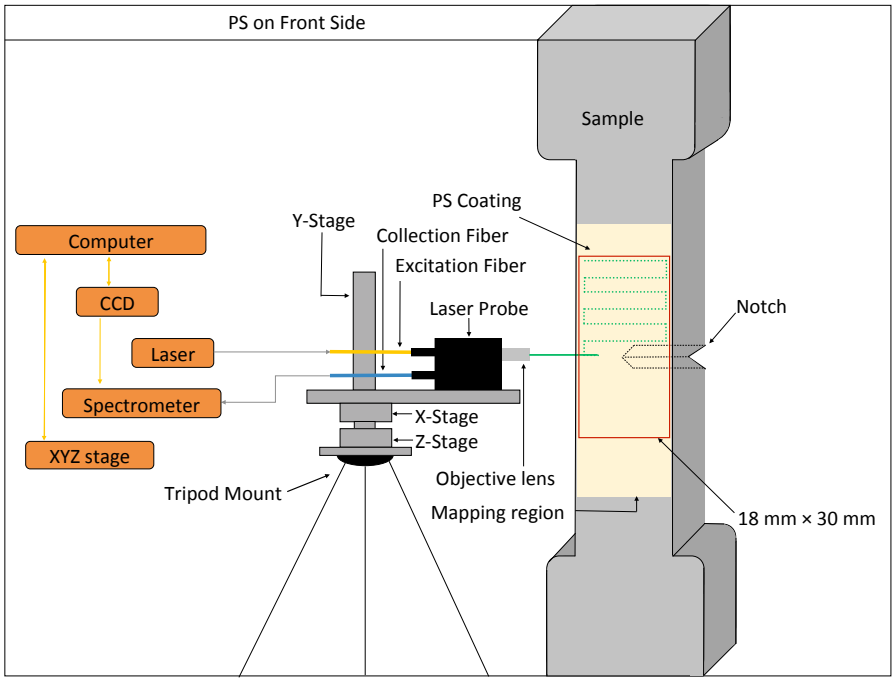

Figure 2.6: The experimental setup is presented in this schematic. Note that the aluminum sample is enlarged to clearly show the PL point-wise scan pattern.

A laser power output of 30.1 mW and 10.6 mW for the 1 vol% and 10 vol% samples, respectively, were used to excite the α-alumina nanoparticles in the PS coatings of both samples during loading. The laser power was chosen based on the spectral emission of the PS coatings, which is dependent on the amount of α-alumina nanoparticles present within those coatings. The PL scans were taken at each hold with a map size of 18 mm $\times$ 30 mm with spatial resolution of 200 μm.

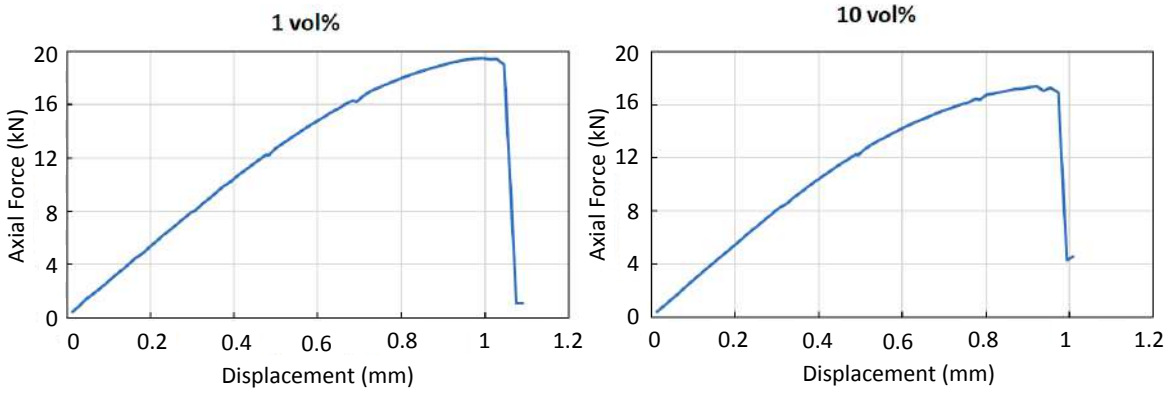

Figure 2.7: Load-displacement response of the Al-2024 tensile sample with stress sensing coating with 1 vol% and 10 vol% α-alumina nanoparticles.

Figure 2.7 shows the tensile response of the Al-2024 tensile specimens with 1 vol% and 10 vol% PS coatings. Similar stiffness was measured from both tests, which indicated that the coating had no effect on how the aluminum specimens responded to the applied tensile load. The results presented here are focused on the photo-luminescent measurements from the coatings during the tensile tests. An example signal response, in the form of R-lines, from each sample are shown in Figure 2.8. The R-lines correspond to the PL scan of one point on each sample at zero applied load. The R1 peak positions from both PS coatings are at 14,402 cm^{-1} at zero load. The peak positions are used as a reference to determine the peak shifts in response to the applied tensile load on the samples. The intensity count was found to be affected by the volume fraction of α-alumina nanoparticles in the coating. Specifically, the intensity from the

coating with 10 vol% α-alumina nanoparticles had almost double the intensity compared to the coating with 1 vol% of α-alumina nanoparticles.

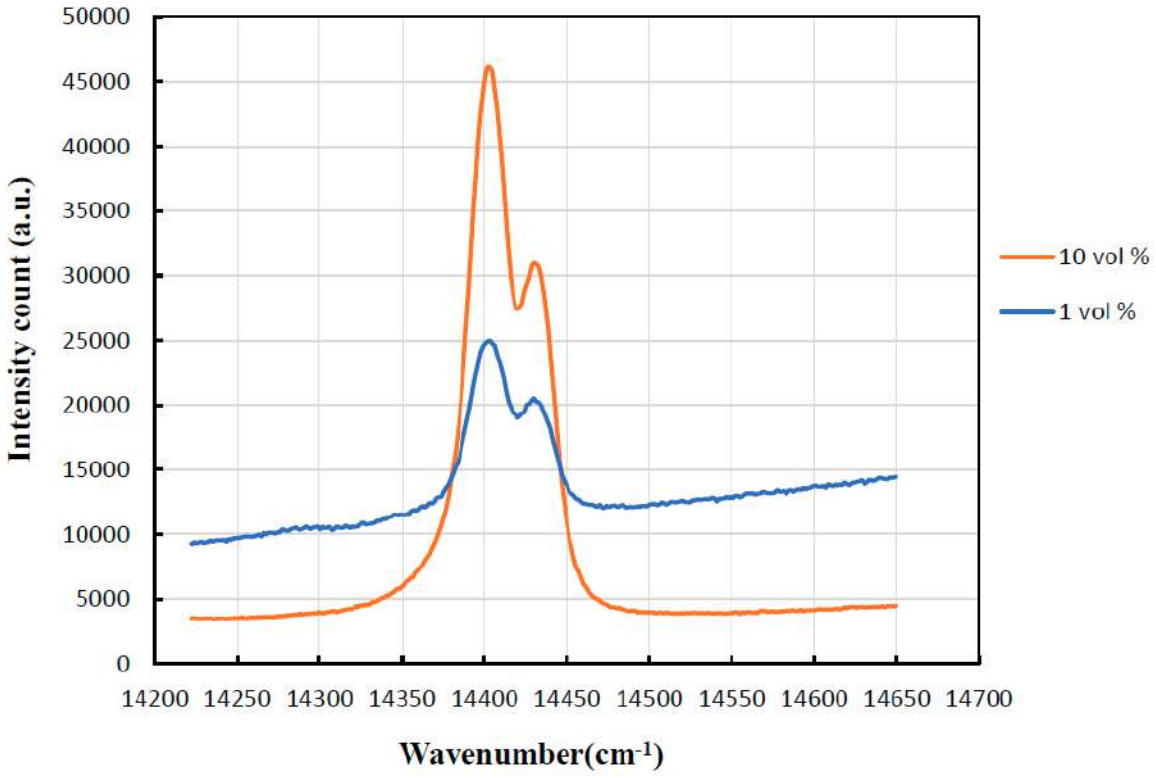

Figure 2.8: R-lines obtained from each sample at zero applied load.

The peak shift maps obtained from the PL scans on the coated surface, on the opposite side of the notch on each sample, are shown in Figure 2.9 for each load step until failure. These maps were plotted from 90 $\times$ 150 point-wise scans to cover an area of 18 mm $\times$ 30 mm at a spatial resolution of 200 μm. They indicate the full field stress state of the coating (and therefore the substrate) for each area that was mapped. A higher or rightward peak shift

indicates larger tensile stress. By comparing the peak shift maps for increasing loads, it is seen that both coatings showed signs of gradually increasing tensile stress, which correlates with the tensile strains captured by DIC, as shown in Figure 2.9. It was observed that the stress is relatively uniform on the surface up to about 8 kN of load for the 10 vol% and 12 kN for the 1 vol%. However, the peak shift map from the 10 vol% PS coating was able to capture the effect of the stress concentration associated with the subsurface notch earlier compared to the 1 vol% PS coating. Additionally, the 10 vol% PS coating captured initial damage progression of the subsurface notch before DIC, which captured initial damage progression at 12 kN. The notch effect was observed in the peak shift maps of the 10 vol% PS coating starting at 8 kN load. The down shifts were observed in the peak shift maps starting from the 8 kN load until post failure due to the stress concentration arising from the subsurface notch that causes stresses to be redistributed around the notch as the load is applied. This observation indicates that the PS coating is capable of detecting the location of subsurface damage initiation. Furthermore, the size of the stress concentration area due to the subsurface damage showed more prominently and compared well with the notch size on the peak shift maps from the 10 vol% PS coating as compared to the maps from the 1 vol% PS coating. Overall, the observed stress state of the coating was found to qualitatively resemble that expected from the global loading in the tensile specimen with a subsurface notch.

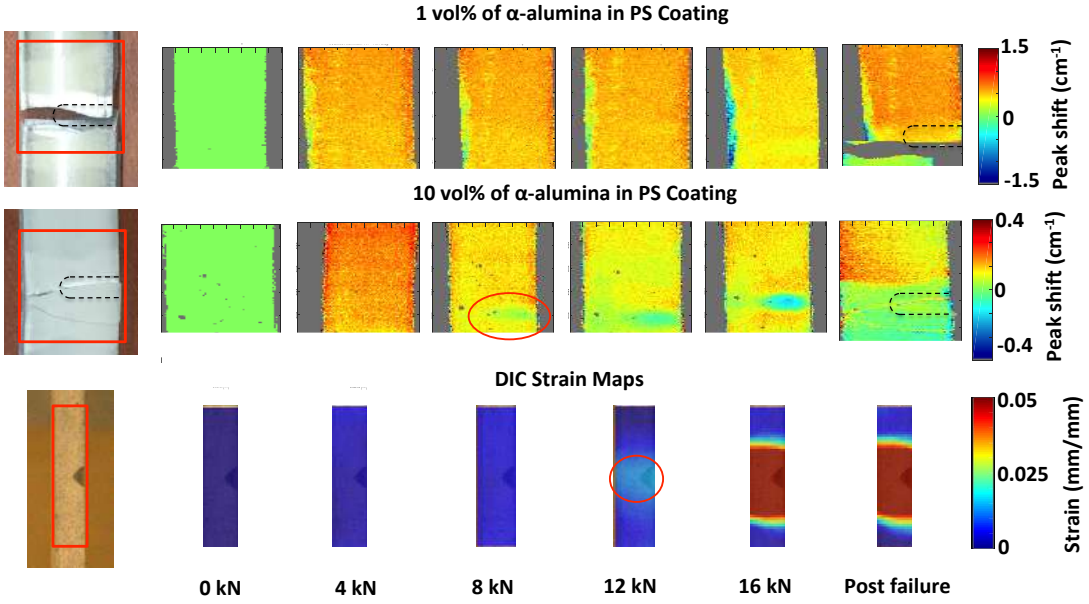

Figure 2.9: Images of the mapped regions of the samples are shown alongside the corresponding R1 peak shift maps (top and middle rows) and DIC strain maps (bottom row) with increasing load. Damage progression of the subsurface notch was detected by the PS coating with 10 vol% alumina at 8 kN before DIC detected damage progression at 12 kN. The PS map dimensions are 18 mm $\times$ 30 mm. DIC maps were taken from the center of the side of the sample, which was 4.826 mm in width.

PS coatings with 1 vol% and 10 vol% α-alumina nanoparticles in epoxy matrix were applied to Al-2024 tensile substrates for stress sensing and damage detection. PL scans were taken during the tensile tests using a custom-made portable piezospectroscopy system. The coatings were capable of determining full-field stress, including the stress concentration due

to the subsurface notch on the aluminum substrates. Further, the PS coating with higher volume fraction (10 vol%) of α-alumina nanoparticles showed higher stress sensitivity than the PS coating with lower volume fraction (1 vol%) of α-alumina nanoparticles. The 10 vol% PS coating was able to capture the notch effect earlier and the notch size more closely than the 1 vol% PS coating. To conclude, the PS coating can provide high spatial resolution images of stress fields and damaged zones specifically when the damage is subsurface or hidden such as on internal surfaces of aerospace structures.

The results discussed in this section have shown that the PS coating's capability in sensing the underlying substrate stress and damage is not only limited to composites, but can also work on metallics. It has demonstrated sensitivity to stress and ability to detect damage progression prior to failure of the metallic substrate, particularly for the PS coating with 10 vol% alumina. The results also show that stress sensitivity increases with increasing particle volume fraction. Since the PS coating has successfully demonstrated stress sensing on metallics, the paint-based PS coating stress sensing capability on metallics will be assessed in this study. Although 10 vol% was the greatest volume fraction tested on a metallic substrate, a paint-based PS coating with 20 vol% alumina will still be used for stress sensing on a metallic substrate to achieve greater sensitivity.

2.4 Selection of Polymer for Coatings

In all tests pertaining to stress-sensing coatings to date, a single polymer material (epoxy resin) was used as the matrix of those coatings. In this work, the PS coating needed to be designed such that it can be used as a paint in external structural parts of an aircraft while being readily available for on-the-field NDE. Since the material sensor configuration used for the alumina-epoxy PS coating was shown to be a working configuration, 20 vol% of α-alumina nanoparticles with 150 nm average particle size and 99.8 % purity were embedded into the paint. The choice of polymer matrix was selected based on the following criteria: material system commonly used on aircraft, transparency to achieve optimal photoluminescence signal from the embedded particles, and the layer of the aircraft paint system the α-alumina particles would be embedded in.

The paint-based PS coating is intended to be placed on the outermost layer of the aircraft paint system to allow immediate access for obtaining photoluminescence signal from the coating. Thus, a topcoat material for the outermost layer of the aircraft paint system had to be selected. Most commercial aircraft use Desothane®HS CA8000/B900A clear topcoat, which is a high solids polyurethane coating that is used to protect the exterior of aircraft. Since this topcoat is colorless, it also meets the criteria of having transparency for optimal photoluminescence signal. Thus, Desothane®HS CA8000/B900A clear topcoat was selected as the matrix for the paint.

CHAPTER 3
MANUFACTURING OF THE PAINT-BASED PIEZOSPECTROSCOPIC COATING

3.1 Design Requirements and Goals

The stress sensing material must be designed such that it can be implemented onto aerospace structures for structural health monitoring. Previous work has integrated α-alumina nanoparticles into an epoxy matrix to form the stress sensing, or piezospectroscopic (PS), coating since epoxy does not interfere with luminescence emission and adheres well to substrates. Although this coating has demonstrated that it can sense the early onset of damage at the subsurface level [1, 65], it still needs to be assessed for ease of application on aircraft surfaces. It is known that 20 % volume fraction of α-alumina nanoparticles that are 150 nm in diameter in the stress sensing material has achieved the required stress sensitivity. Thus, this particle loading was taken into consideration when designing a paint-based PS coating. For this work, the α-alumina nanoparticles were implemented into industry standard, high solids (HS) polyurethane clear topcoat (PPG Aerospace) that is typically used to protect the exterior of aircraft to create the paint-based PS coating, so that it will have practical use on aircraft structures. In this chapter, the process for manufacturing this paint-based coating was explored prior to testing to ensure that the modified configuration retains its stress sensing capability.

Determining the ideal fabrication procedure for the paint-based PS coating is imperative, so that the α-alumina nanoparticles within the paint are as uniformly dispersed as possible. Dispersion is an important factor to consider when manufacturing nanomaterials to reduce the

onset of stress concentrations and avoid premature failure [46]. The paint should be quick and simple to apply on substrates and comply with standard practices of applying paint on aircraft in industry. Mostly importantly, in order for this paint to be efficient for use, it must have high sensitivity and be able to sense the stress and damage at the surface and subsurface level of the substrate. Dispersion and adhesion to the substrate are important parameters for this. For stress sensing to be possible, the paint must emit sufficient luminescence emission, which means that the matrix should not block any emission coming from the α-alumina nanoparticles. This was one of the other reasons why the HS polyurethane clear topcoat was chosen as the matrix as it is transparent and, thus, will not interfere with the spectral emission of the nanoparticles. At the same time, the paint-based PS coating must adhere well to the substrate during load tests in order to track the progression of stress up to the failure of the substrate.

Two iterations of the paint-based PS coating fabrication were manufactured in collaboration with Boeing Research & Technology. For the first iteration, different combinations of equipment were used to make the paint and determine which pieces of equipment were most suitable for mixing and applying the paint. Once those were determined, they were used to make the second iteration of the paint-based PS coating recipes. For this iteration, several mixing methods were performed, and a dispersant was added to the mixture to improve the particle dispersion. Flowcharts summarizing the paint-based PS coating processing approaches used in each iteration are provided in Figures 3.1 and 3.4.

3.2 Equipment Selection for Manufacturing Paint-Based Piezospectroscopic Coating

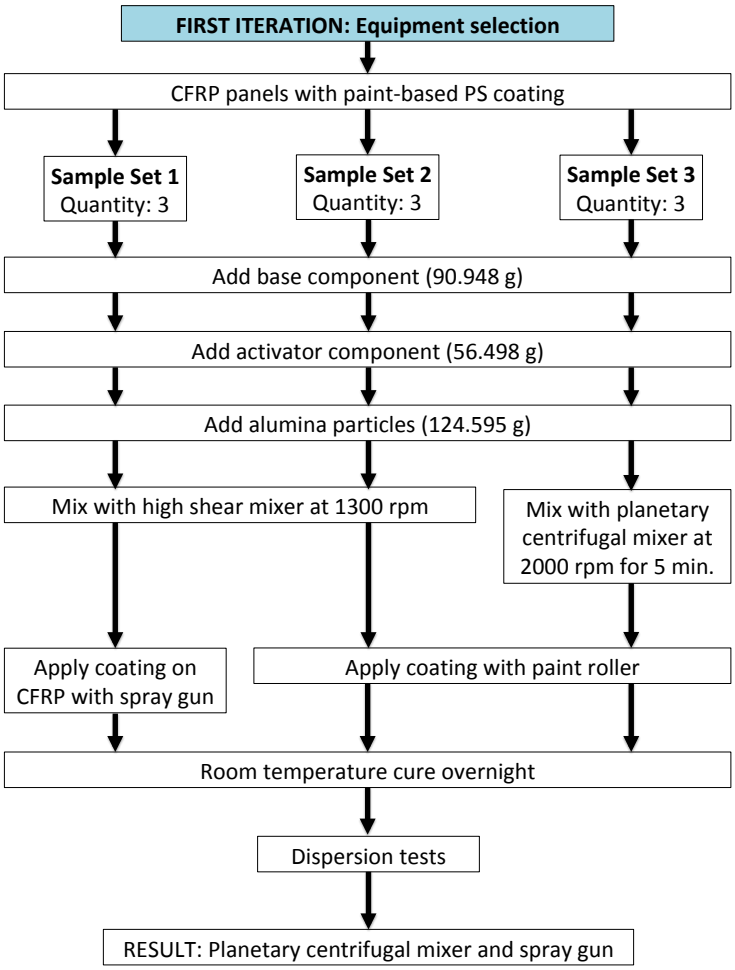

Figure 3.1: Flowchart showing the paint-based PS coating process approaches used in the first iteration. The selected equipment were implemented into the second iteration of coating manufacturing.

3.2.1 Coating Mixing and Application Using Varying Equipment Combinations

Three sets of samples were manufactured using varying equipment combinations, as shown in Figure 3.1. Each set consists of three samples with different paint configurations to compare luminescence emission and particle dispersion due to the manufacturing method. These samples consisted of composite substrates with paint made of 20 vol% α-alumina nanoparticles (Inframat Advanced Materials LLC) embedded in high solids (HS) polyurethane clear topcoat (PPG Aerospace). The α-alumina nanoparticles have an average particle size of 150 nm, and 99.8 % purity. For each sample set, the paint was manufactured using different combinations of equipment for paint mixing and application, which are summarized in Table 3.1. The components of the paint were added in the same order for each sample set. The base component of the HS polyurethane clear topcoat was first; the activator component of the HS polyurethane clear topcoat was second in the mixture; and the third component that went into the mixture was 20 vol% of α-alumina nanoparticles.

Table 3.1: Summary of paint manufacturing methods

Sample Set Number	Mixing Method	Application Method
1	High shear mixing	Spray gun
2	High shear mixing	Paint roller
3	Planetary centrifugal mixing	Paint roller

3.2.2 Photoluminescent Signal Response and Particle Dispersion of Coatings Made with Varying Equipment

Photoluminescence (PL) scans were taken to collect data and produce dispersion maps that show the intensity at each point of each sample. These maps showed characteristics of the α-alumina particle dispersion within the HS polyurethane matrix. PL data was collected in a 128 $\times$ 128 point grid , which corresponded to a measurement area of 51.2 mm $\times$ 51.2 mm and a spatial resolution of 0.4 mm. Collection time per point and total collection time for one representative sample from each set are shown in Table 3.2.

Emission quality of each paint-based PS coating configuration was assessed based on the intensity of the R-lines (Figure 3.2) and signal-to-noise (SNR) (Table 3.2) since a strong PL signal is necessary for piezospectroscopy. The median SNR was obtained from the median of all of the spectra from the surface map of each sample. Particle dispersion maps were also assessed to determine which paint manufacturing method dispersed the particles as uniformly as possible across the substrates since agglomerations would affect the mechanical properties of the paint. Each map consisted of R-lines (Figure 3.2) from 16,384-point locations.

Table 3.2: Experimental parameters of one representative sample from each set

Sample ID	Collection Time per Point	Total Collection Time	Median SNR
1-1	20 ms	14 minutes	109.49
2-1	40 ms	20 minutes	55.75
3-1	40 ms	20 minutes	127.53

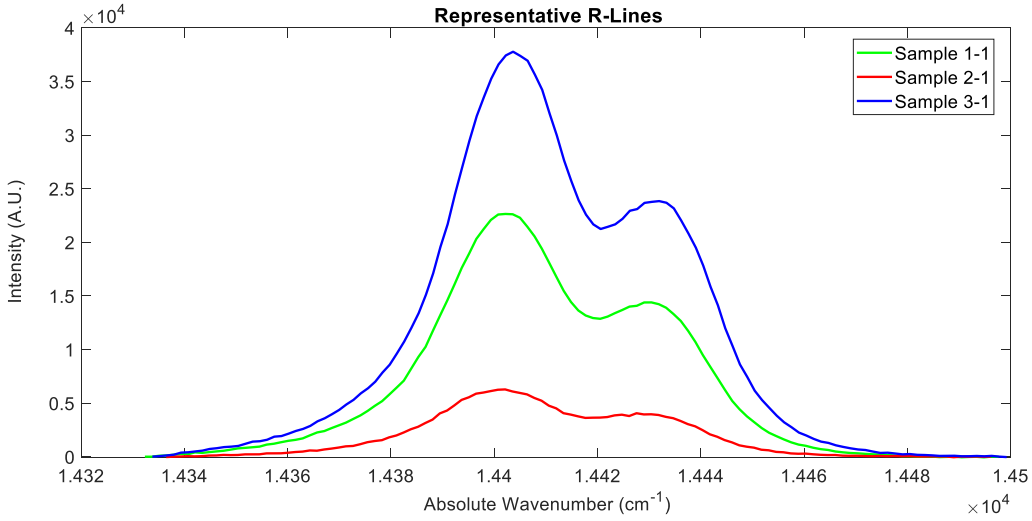

Figure 3.2: Representative R-lines for each sample.

The quality of the R-lines can be determined using the median SNR. Higher median SNR correlates with higher median intensity. Based on the results shown in Figure 3.2 and Table 3.2, the samples from set 3 had the highest median SNR and intensity. The differences in intensity within each of the representative samples are shown in the dispersion maps in Figure 3.3. Each map has dimensions of 51.2 mm $\times$ 51.2 mm and were normalized to show how much they deviate from the maximum intensity measured out of all the samples. Overall, they showed that the dispersion of the α-alumina nanoparticles within the HS polyurethane matrix varied greatly.

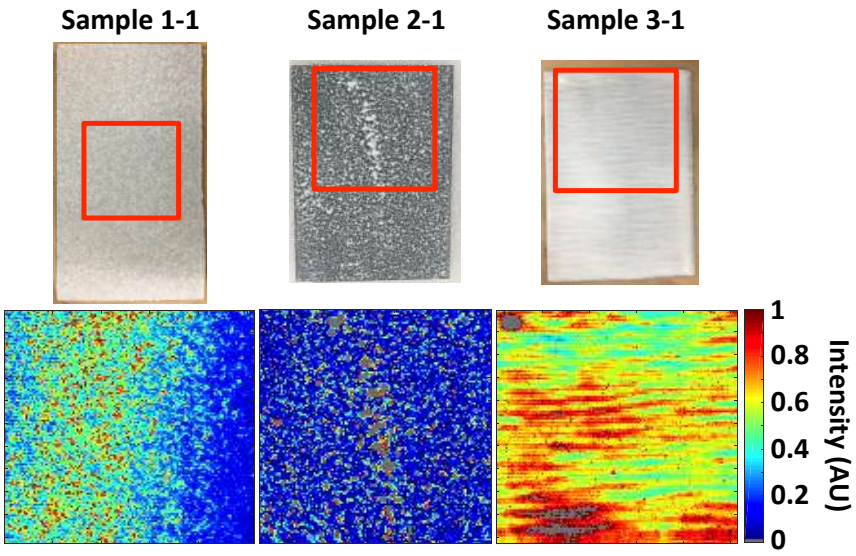

Figure 3.3: Representative samples (top row) with their corresponding normalized dispersion maps (bottom row) showing α-alumina nanoparticle dispersion. Sample 1-1 was made using high shear mixing and spray gun. Sample 2-1 was made using high shear mixing and a paint roller. Sample 3-1 was made using planetary centrifugal mixing and a paint roller.

The dispersion map for the first sample set (Figure 3.3) showed that there were agglomerated spots in a speckle-like pattern. This pattern may have been attributed to the way in which the paint was applied. It was noted that the α-alumina nanoparticles congested the nozzle of the spray gun, causing uneven distribution of the paint. Thus, some areas of the sample had more agglomerated areas than others, as indicated by the leftmost area of the dispersion map. This variation in dispersion makes the paint, processed in this way, non-ideal for stress sensing.

For the second sample set (Figure 3.3), the dispersion map shows relatively low intensity points due to poor dispersion of the α-alumina nanoparticles. The paint roller allowed for ease of application, but the particles were still not mixed well enough to be dispersed as evenly as possible. The grey streak in the middle of the map corresponds to the white streak on the actual sample, which indicated that there was high agglomeration of particles. This grey streak indicates points on the sample with invalid signal intensity due to the concentration of α-alumina nanoparticles being too high at those points causing saturation. Thus, this paint configuration would not be ideal for stress sensing due to high agglomerations.

For the third sample set, the planetary centrifugal mixing method was used instead of the cowl blade mixing method to mix the α-alumina nanoparticles with the HS polyurethane. Similar to the paints for first and second sample sets, the paint for the third sample set had areas of high particle agglomeration, as shown in the dispersion map for Sample 3-1 (Figure 3.3), which indicated that more improvements to the manufacturing procedure needed to be made to achieve more uniformity in particle dispersion. Additionally, similar to Sample 2-1, Sample 3-1 had saturation points, particularly at the top- and bottom-left corners of its dispersion map, that correspond to very high presence of α-alumina nanoparticles. Despite this manufacturing defect, the paint for the third sample set had the highest median intensity and SNR out of all the samples tested. These characteristics made this paint the most ideal configuration for further stress sensing tests for this study.

3.3 Processing Approach and Thickness Selection for Manufacturing Paint-Based Piezospectroscopic Paint

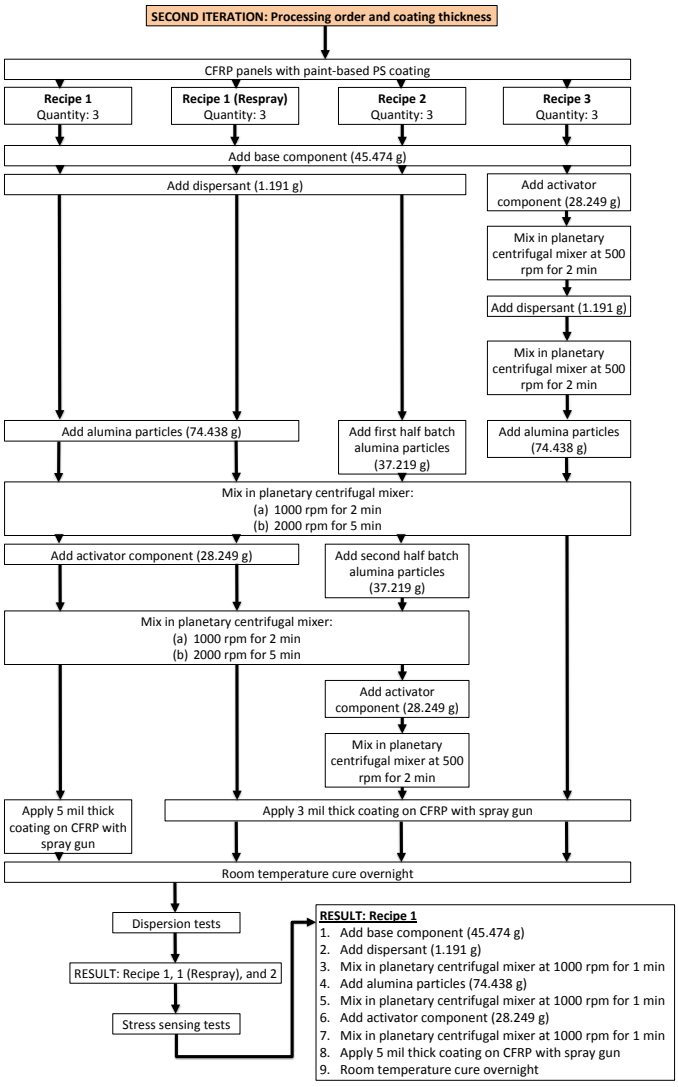

Figure 3.4: Flowchart showing the paint-based PS coating process approaches used in the second iteration. The selected coating thickness and processing order were used to manufacture the coating for the ASTM standard substrates for further stress sensing tests.

3.3.1 Coating Manufacturing Using Varying Recipes

The paint recipe was revised to include a dispersant that would improve particle dispersion and reduce agglomerations and sedimentation. Typically, aircraft paint is applied with spray equipment. It was observed that, during the first iteration, the α-alumina nanoparticles would agglomerate at the nozzle of the spray gun, which caused difficulty in spraying. This observation suggests that a dispersant would be needed to reduce the agglomerations. Solplus^{TM} R710 (Lubrizol Corp.) was specifically chosen as the dispersant for the paint-based PS coating due to its compatibility with organic matrices, such as polyurethane in this case, and its versatile use for dispersing organic and inorganic fillers. From the first iteration, it was found that the planetary centrifugal mixer (THINKY Corp.) was most effective in mixing the paint components as uniformly as possible. Thus, it was decided that this mixer would be used for the second iteration of the paint-based PS coating. Lastly, the curing procedure, as outlined in the PPG Aerospace technical data sheet, was kept consistent for all of the paint made for this second iteration. The paint-based PS coating was dried overnight (or at least 8 to 10 hours) at room temperature. Three sets of samples were made for the second iteration of the paint-based PS coating. The manufacturing procedure differed for each set due to changes in the mixing steps and how each component of the paint is added to the mixture paint-based PS coating.

For the first set of samples (Recipe 1 and Recipe 1 (Respray) in Figure 3.4), the dispersant was added into the clear topcoat's base component first. Next, 20 vol% of the α-alumina nanoparticles was added into the mixture. These three components were mixed using the plan-

etary centrifugal mixer. The planetary centrifugal mixer was set to perform two steps: mix for two minutes at 1000 rpm and then mix for 5 minutes at 2000 rpm. Then, the clear topcoat's activator component was included in the mixture. The mixture was placed in the planetary centrifugal mixer, and the two mixing steps were done again. Three samples were made using Recipe 1, and three other samples were made using Recipe 1 (Respray). Samples that were made using Recipe 1 have a coating thickness of 5 mil, while samples that were made using Recipe 1 (Respray) have a coating thickness of 3 mil.

In comparison to the first set of samples, the paint for the second set of samples (Recipe 2 in Figure 3.4) was made by adding the 20 vol% α-alumina nanoparticles in two smaller batches. First, the dispersant was added into the clear topcoat's base component. Next, the first half of the α-alumina batch was added into the mixture. This mixture was stirred in the planetary centrifugal mixer using two steps: mix for 2 minutes at 1000 rpm and then mix for 5 minutes at 2000 rpm. After mixing, the second half of the α-alumina batch was added. The mixture was stirred again in the planetary centrifugal mixer using the same two steps. The activator component was then added to the mixture. The planetary centrifugal mixer was used again to stir the paint for 2 minutes at 500 rpm.

For the third set of samples (Recipe 3 in Figure 3.4), the activator component was added to the base component first as a different approach from the other two methods in which the activator was the last component added to the mixture. These two components were mixed in the planetary centrifugal mixer for 2 minutes at 500 rpm. Next the dispersant was added to the mixture. This mixture was stirred again for 2 minutes at 500 rpm in the planetary centrifugal

mixer. Then, 20 vol% of α-alumina nanoparticles were added to make the paint. This paint was mixed in the planetary centrifugal mixer once more, but with two steps: mix for 2 minutes at 1000 rpm and then mix for 5 minutes at 2000 rpm.

It was noted that the mixing steps would cause the planetary centrifugal mixer to overheat due to using a high revolution speed (maximum at 2000 rpm) and long mixing times. This, specifically, applied to the steps where 1000 rpm for 2 minutes and 2000 rpm for 5 minutes were implemented. Thus, for the selected processing approach, the order in which the coating components were added would be kept the same, but the mixing steps would be slightly modified to prevent overheating while ensuring adequate mixing, as shown in Figure 3.4.

3.3.2 Photoluminescent Signal Response and Particle Dispersion of Coatings Made with Varying Recipes

The intensity maps (Figure 3.5), which show the particle dispersion of the paint, were obtained using photoluminescence (PL) spectroscopy. PL data was collected in a 128 $\times$ 128 point grid, which is a map area of 51.2 mm $\times$ 51.2 mm, and a spatial resolution of 0.4 mm was used. For each map, the total collection time was approximate 20 minutes. The laser power and exposure time were 15 mW and 40 ms, respectively.

Figure 3.5 shows the particle dispersion within the paint-based PS coating for each sample set. Table 3.3 shows the median SNRs, intensities and luminosities for each sample set. Through qualitative assessment of the intensity maps, the second iteration paint-based PS coat-

ing, overall, shows improvement in the particle dispersion in comparison to the particle dispersion in the first iteration paint-based PS coating (Figure 3.3) since there are less visibly large agglomerations. However, some small agglomerations were observed especially from samples with Recipe 2 and Recipe 3. For Recipe 1, agglomerations were noticeable on the right edge of samples 1 and, away from the edge, a gradient in intensities indicated reduced presence of particles in the coating from the top to the bottom of the scanned area. Sample 2, while it had an agglomerated area at the right edge, had more uniformity in dispersion away from the edge with the exception of one agglomerated spot. The particles in Sample 3 were more uniformly dispersed than those in samples 1 and 2. For Recipe 1 (Respray), particle dispersion was fairly uniform with the exception of Sample 11, which had some agglomerated spots. Comparing the samples with coating Recipe 1 to samples with coating Recipe 1 (Respray), the dispersion maps show that greater coating thickness correlates with higher intensities due to greater depth and volume of coating probed for a given volume fraction of alumina particles. However, regardless of thickness, both coating thicknesses had adequate intensities to discern any dispersion characteristics. It was observed that the thicker coating was more prone to higher agglomerations, particularly at the edge of each panel.

Assessment of the median SNR, intensity, and luminosity for each recipe was based on the criteria used to assess the median values for the alumina-epoxy PS coatings with varying particle content (Section 2.2). Higher median SNR, intensity and luminosity reduces uncertainty in the peak position and results in smoother R-lines; thus, leading to more distinctive peak shifts for stress sensing. It was observed that the samples with paint Recipe 1 had the highest median

SNR, intensity and luminosity out of all of the recipes tested due to it being greater in thickness and, thus, greater concentration of the coating.

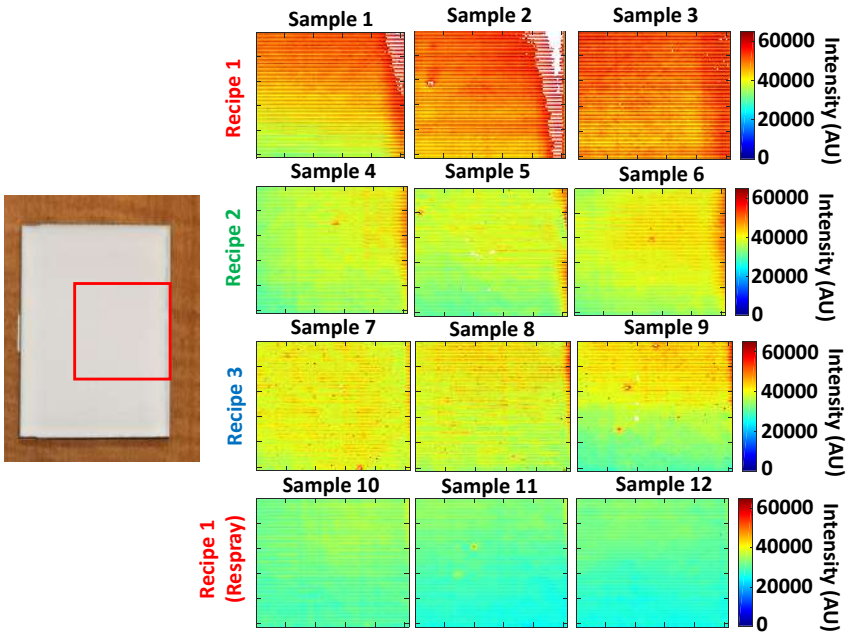

Figure 3.5: Comparison of paint-based PS coating particle dispersion via PL spectroscopy. The sample shown on the left is 101.6 mm $\times$ 76.2 mm.

Table 3.3: Comparison of median SNRs, intensities and luminosities for each sample set.

Results	Recipe 1	Recipe 1 (Respray)	Recipe 2	Recipe 3
Median SNR	132	117	124	125
Median Intensity	49,102 AU	29,619 AU	36,573 AU	38,914 AU
Median Luminosity	1,227,543 counts/sec	740,464 counts/sec	914,319 counts/sec	972,860 counts/sec

Based on the luminescence intensity results, the choice of paint processing approach was down selected to Recipes 1, 1 (Respray), and 2 due to having good dispersion, whereas Recipe 3 had the worst dispersion due to the presence of agglomerated spots. Since Recipe 1 and Recipe 1 (Respray) have the same processing approaches but different thicknesses, their dispersion are further assessed quantitatively. For each paint-based PS coating thickness, a histogram of dispersion was plotted, as shown in Figure 3.6, with the plots of the samples with the same coating thickness overlaying each other. Figure 3.6 also includes a global plot to compare the dispersion histograms of both thicknesses.

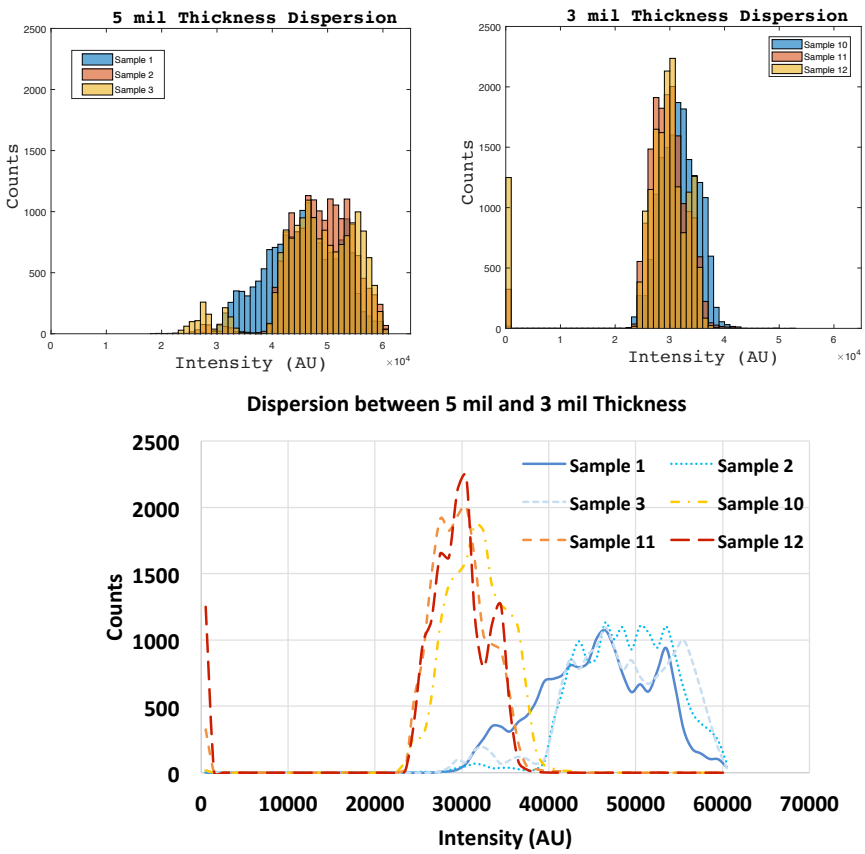

Figure 3.6: Histograms were plotted to show frequency distribution of intensities for different paint-based PS coating thicknesses. ”Counts” pertain to the number of instances of an R1 intensity value.

The histogram for the paint-based PS coating with 5 mil thickness shows a skewed left distribution for all samples. This indicates that most of the data points fall within the range of 40,000 AU and 60,000 AU, while a few data points were less than 40,000 AU. This distribution can especially be seen in Samples 1 and 2 in Figure 3.5, where there is a gradient of intensities

going from right to left, whereas a subtle gradient in intensities is seen in Sample 3. On the other hand, the histogram for the paint-based PS coating with 3 mil thickness shows a narrow and fairly symmetric distribution between 20,000 AU and 45,000 AU with the exception of a few outlier points that have very little to no intensity. These outlier points could indicate areas of the coating with little to no particles, which is especially noticeable in Samples 11 and 12 (Figure 3.5) since a decrease in intensities can be seen from top to bottom of the map scans. Despite this, the overall distribution of the 3 mil thick coating indicates that it has better dispersion than the 5 mil thick coating. Although the dispersion is not as good as the 3 mil thick coating, the 5 mil thick coating was still selected due to it having higher intensity and SNR.

Next, the dispersion the paint-based PS coatings made with Recipes 1 and 2 are further assessed here. Coating thickness are kept consistent for this comparison; thus, samples made with the Recipe 1 (Respray) coating are compared to those made with the Recipe 2 coating as they both have a thickness of 3 mil. Similar to how the coating thicknesses were assessed, the recipes will be compared based on quantitative results from the dispersion histograms and PS coefficient plots. Figure 3.7 shows a histogram of dispersion for each processing approach (recipe), with the plots of the samples with the same coating recipe overlaying each other. A global plot is also shown in Figure 3.7 to compare the dispersion histograms of both recipes. The dispersion histogram for Recipe 2 has a slightly wider spread of intensities than Recipe 1 and has counts that are more pronounced between the intensities of 30,000 AU and 40,000 AU, which most likely are associated with agglomerated spots on the paint-based PS coating

made with this recipe, as shown in Figure 3.5. Quantitatively, this shows that Recipe 1 is better dispersed.

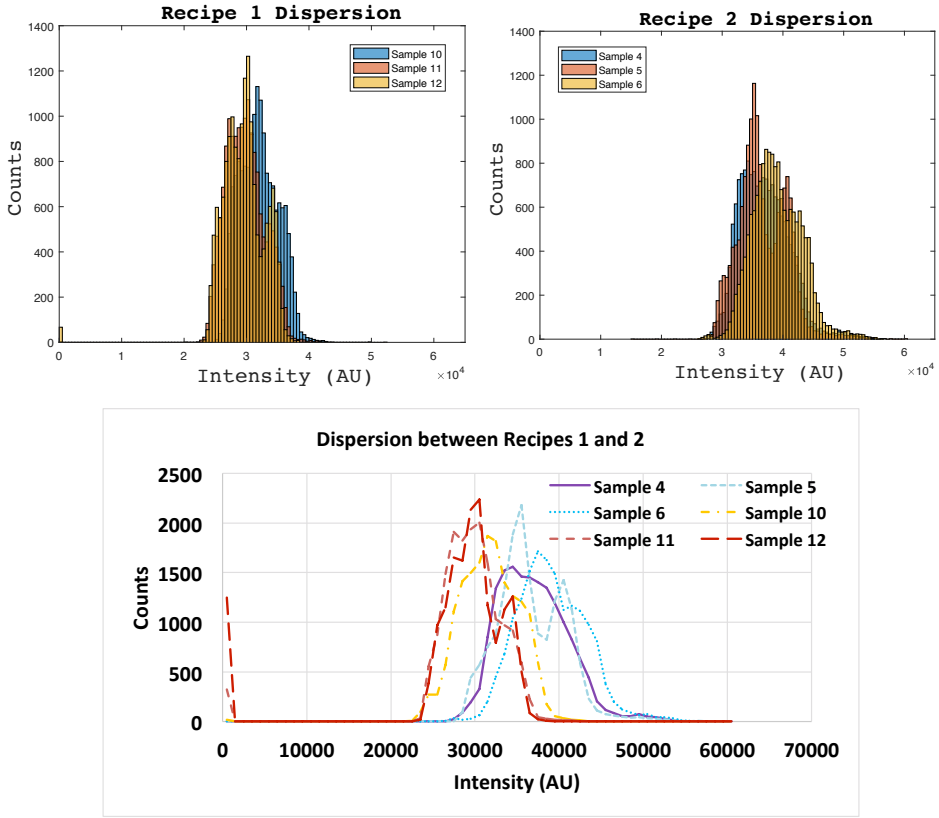

Figure 3.7: Histograms were plotted to show frequency distribution of intensities for processing approaches Recipes 1 and 2. ”Counts” pertain to the number of instances of an R1 intensity value.

Comparisons of the coating thickness and recipes, particularly those that showed good dispersion qualitatively, were made to further assess their dispersion quantitatively. The histograms that compared the 3 mil and 5 mil thick coatings showed that having a thicker coating

ensures that it has higher intensity and SNR while having acceptable dispersion. Based on the comparison of dispersion between recipes, Recipe 1 had better dispersion than Recipe 2 since Recipe 2 had a wider spread of intensities and more pronounced counts that are indicative of highly agglomerated spots. Combining the results of the thickness and recipe comparisons, using Recipe 1 with a thickness of 5 mils would be ideal in terms of particle dispersion. However, particle dispersion was not the only factor to consider for selecting a processing approach. The coating, most importantly, needed to be able to sense stress. Thus, load tests were done to test the stress sensing capability of the coatings made with Recipes 1, 1 (Respray), and 2.

3.4 Selection of Paint-Based Piezospectroscopic Coating Based on Stress Sensing Capability

The coated panels made with Recipes 1, 1 (Respray), and 2 were cut into tensile coupons to test them for stress sensing capability and to ensure that the coatings remained adhered to the substrate during the load tests. In this section, the effect of thickness and the effect of different coating recipes are assessed for stress sensing.

3.4.1 Experimental Setup for Tensile Testing

Panels with Recipes 1, 1 (Respray), and 2 paint-based PS coating were cut into tensile coupons based on the suggested dimensions provided by ASTM 3039 [66]. Each coupon had dimen-

sions of 101.6 mm $\times$ 10.16 mm $\times$ 2.54 mm. The coupons were prepared with medium graded emery cloth on the gripping ends and mounted onto a servohydralic MTS universal testing machine with serrated grips. Displacement control was used with a crosshead speed of 0.2 mm/min and a limit of 14 kN. During ramp up, DIC images were captured to monitor the strain. At each 1 kN load increment, each coupon was held at a constant displacement (Figure 3.8) to collect PS data using a neon-argon laser at a wavelength of 532 nm as the excitation source. The hold time for each sample was 25 seconds for each map scan. The map scan was taken at the center of each sample with dimensions of 12.8 mm $\times$ 4.8 mm. Figure 3.9 shows the experiment setup for tensile testing of the paint-based PS coated sample and data collection using the PS and DIC systems. Table 3.4 provides the mechanical, PS and DIC parameters that were used for this test.

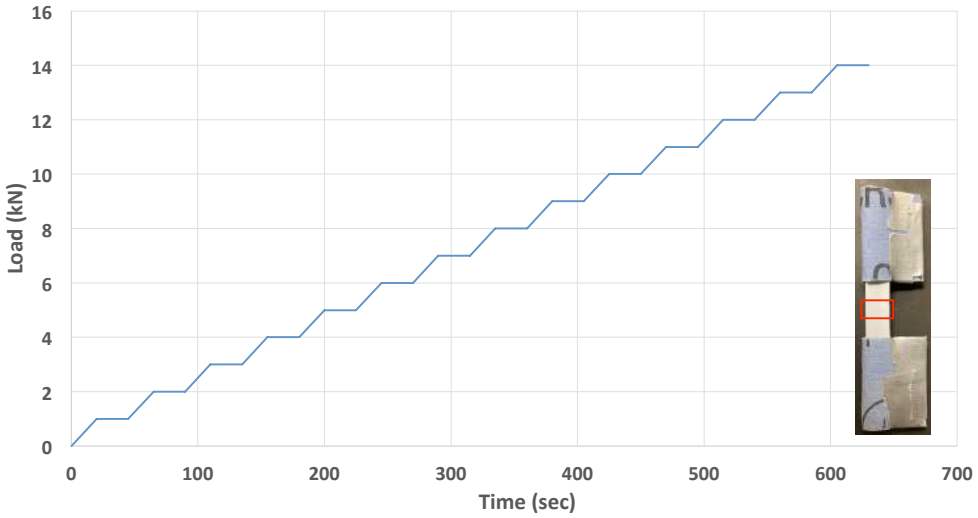

Figure 3.8: A load step plot showing when displacement holds were implemented to perform the PS map scans. Displacement holds were done at 1 kN load increments, and the samples were taken up to 14 kN.

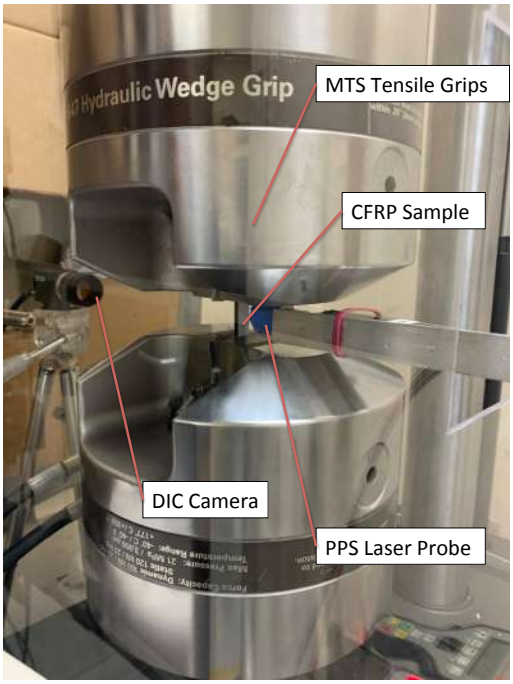

Figure 3.9: An experiment setup for tensile testing of CFRP samples with paint-based PS coating is shown here. The portable PS system was used to collect PL data from the paint-based PS coating side of the sample, while a DIC camera was used to collect strain data from the speckle-patterned paint side of the sample.

Table 3.4: Mechanical, PS and DIC parameters for tensile testing of the CFRP samples with different paint recipes and thicknesses.

Mechanical Test Parameters	
Displacement rate	0.2 mm/min
Grip pressure	6 MPa
Load step	1 kN
Maximum load	14 kN
PS Data Collection Parameters	
Laser power	15 mW
Exposure time	40 ms
Number of exposures per frame	1
Resolution	400 μm
Map size	12.8 mm $\times$ 4.8 mm
Pixel map size	32 points $\times$ 12 points
DIC Data Collection Parameters	
Image capture rate	1 image/sec
Framerate	15 fps
Horizontal bin	1
Vertical bin	1
Resolution	3500 $\times$ 3500

3.4.2 Effect of Coating Thickness and Recipe on Stress Sensing

The peak shift maps that were obtained from each sample are shown in Figure 3.10. These maps serve as an initial check for signs of shifting and detachment of the paint-based PS coating from the substrate. For all of the samples tested, the peak shift maps show leftward shifts, instead of the expected rightward shifts, with increasing tensile load, and this needs to be further investigated. The sample that was made with the 5 mil thick coating showed more discernible shifts than the samples with 3 mil thick coating. This indicates that the sensitivity of the coating increases with thickness.

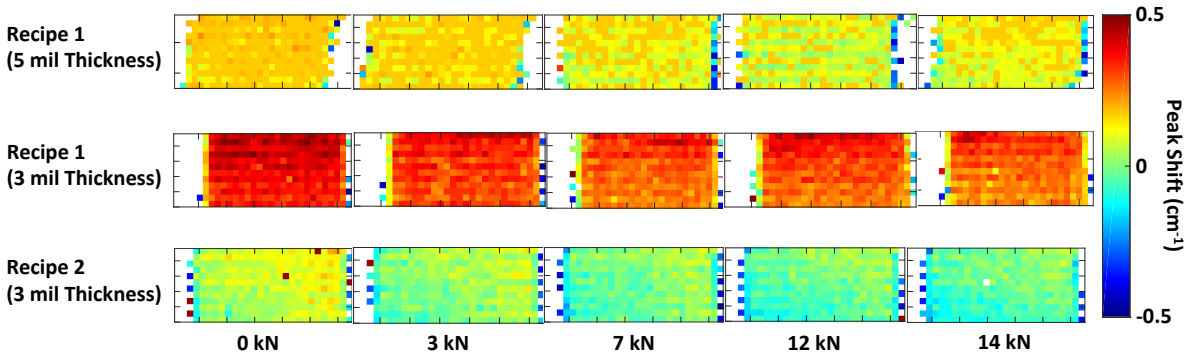

Figure 3.10: Comparisons of the stress states with increasing uniaxial tensile load of paint-based PS coatings with different thicknesses (5 mil and 3 mil) and different processing recipes (1 and 2) that qualitatively show leftward R1 peak shifts from the unloaded condition.

For all the paint-based PS coating recipes that were tested for stress sensing capability, none of them appeared to have detached from the substrate during the load tests based on visual inspection. Despite the R1 peak shifts not shifting rightward as expected when the alumina particles within the coating are subjected to tensile stress, the R1 peaks were still shifting with increasing load. This indicated that the coating is still sensing stress during the load tests, which would not be the case if the coating detached from the substrate. Thus, it can be inferred that the paint-based PS coatings adhered to the substrates during the load tests. However, the reason for the leftward shift trend has yet to be determined and, through further experiments, possible reasons are discussed in Chapter 4.

3.5 Summary of Results

From the first set of samples, it was found that the planetary centrifugal mixer performed best at blending the alumina particles into the polyurethane matrix. However, the paint-based PS coating still needed to be improved for better dispersion and to allow ease of application with a spray gun. For the second set of samples, the planetary centrifugal mixer and spray gun was implemented into the various coating recipes that were made. A dispersant was added into the coating mixture, which helped achieve more uniformity in particle dispersion. Based on qualitative dispersion results, Recipe 3, which had the activator component added into the mixture second as opposed to last like the rest of the recipes, exhibited the worst dispersion due to the presence of multiple areas with high agglomerations. This likely occurred because

the activator serves as a hardener, which was causing the base component to harden before the other components - the dispersant and alumina particles - could mix well in it. Thus, it is best to mix the base component, dispersant and alumina particles together first before adding the activator. Recipes 1, 1 (Respray), and 2 all exhibited good dispersion and were further tested to assess dispersion quantitatively and stress sensing capability.

Thickness and coating recipes were compared and assessed for their dispersion and sensitivity to stress. Based on the results of this chapter, the paint-based PS coating with 5 mil thickness and made with Recipe 1 exhibited the ideal characteristics for a stress sensing coating configuration. Out of the thicknesses and recipes assessed here, Recipe 1 with 5 mil thickness had higher intensity and SNR and did not exhibit discernible anomalies in dispersion. This coating configuration also demonstrated greater sensitivity based on qualitative peak shift results. However, like the other coating recipes tested for stress sensing capability, the peak shifts obtained from the Recipe 1, 5 mil thick coating showed a leftward trend instead of the expected rightward shifts corresponding to tensile stress. Although, by visual inspection, the coating did not show signs of detachment from the substrate, further inspection must be done to determine the cause for the leftward shifts. These leftwards shifts could indicate stress relaxation of the coating, which can be due to micro-damage, weak polymer-to-particle bonding, or temperature effect. In Chapter 4, the Recipe 1, 5 mil thick coating was applied onto a notched aluminum substrate and an OHT CFRP substrate to test its capability of sensing the stress state of different substrate materials and the stress concentrations at the notched and open hole regions. Scanning electron microscopy images of the coating before and after load tests were taken to

inspect it for signs of micro-damage. Peak shift measurements were taken as the paint-based PS coating was heated and cooled to determine the effect of temperature on peak shifts.

CHAPTER 4
STRESS SENSING OF PAINT-BASED PIEZOSPECTROSCOPIC COATING ON NOTCHED METALLIC AND COMPOSITE SUBSTRATES

4.1 Objectives

Paint-based PS coating Recipe 1 and 5 mil coating thickness was selected since it demonstrated sensitivity to stress, good dispersion and good adhesion to the substrate during load tests. This coating configuration was implemented onto larger, ASTM-standard metallic (Al-2024) and composite (CFRP) substrates to determine the coating's sensing capability on different materials. The selection of metallic and CFRP substrates were based on materials that are commonly used on aircraft structures.

4.2 Experiment Setup for Tensile Testing on Notched Aluminum and Open-Hole Tension Composite Specimens

The Al-2024 substrate was made as per ASTM E647 [67], and the CFRP substrate was made as per ASTM D5766 [68]. The Al-2024 substrate had dimensions of 160.02 mm $\times$ 39.88 mm $\times$ 4.06 mm, while the CFRP substrate had dimensions of 304.8 mm $\times$ 38.1 mm $\times$ 3.81 mm. Both substrates were designed with a notch or hole at the center to induce a stress concentration at the notch or hole when the substrates are subjected to tensile load. The notch or hole was implemented before the paint-based PS coating was applied onto the substrates. Each sample

was mounted onto a servohydraulic MTS universal testing machine with serrated grips. Displacement control was used with a crosshead speed of 0.2 mm/min. The PS and DIC systems were used to monitor the peak shifts and strains, respectively, with applied load.

For the coated, notched Al-2024 sample, the PS maps were taken at each load step as shown in Figure 4.1. A higher frequency of data collection was done at lower loads to ensure that peak shifts indicating tensile stress would be captured. Initially, the sample was loaded in increments of 0.5 kN from 0 kN (with MTS grips on) to 3 kN. Then, the sample was loaded in increments of 3 kN from 3 kN to 24 kN. The maximum load, 24 kN, was based on 50 % of the failure load of the substrate. This is to ensure that sufficient tensile stress was applied to the substrate without causing it to fail. The hold time for each PS map scan was 6 minutes, and each map had dimensions of 42.4 mm $\times$ 25.6 mm.

For the coated, open-hole tension (OHT) CFRP sample, the PS maps were taken at each load step as shown in Figure 4.2. A higher frequency of data collection was done at higher loads to ensure that any initiation of damage was captured. The sample was loaded in the following increments: 4 kN from 0 kN (with MTS grips on) to 24 kN, 2 kN from 24 kN to 28 kN, and 1 kN from 28 kN to 32 kN. The sample was then unloaded back to zero using the same load steps going up to compare the stress state of the coating at post-load to that of the coating before load. The maximum load, 32 kN, was based on approximately 70 % failure load of the substrate, which was chosen to ensure that sufficient tensile stress was applied without causing the substrate to fail. The hold time for each PS map scan was 5 minutes, and each map had

dimensions of 25.6 mm $\times$ 25.6 mm. A detailed list of mechanical, PS and DIC parameters that were used are shown in Table 4.1.

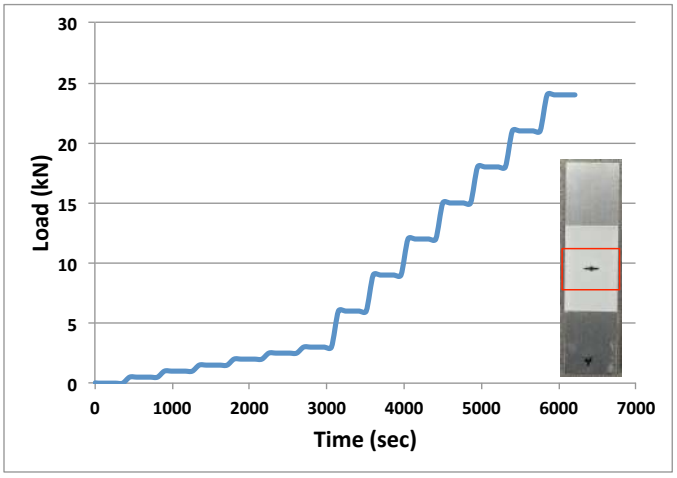

Figure 4.1: A load step plot for tensile testing of the notched Al-2024 sample with paint-based PS coating. An image of the notched Al-2024 sample is shown on the right with the mapped region boxed in red.

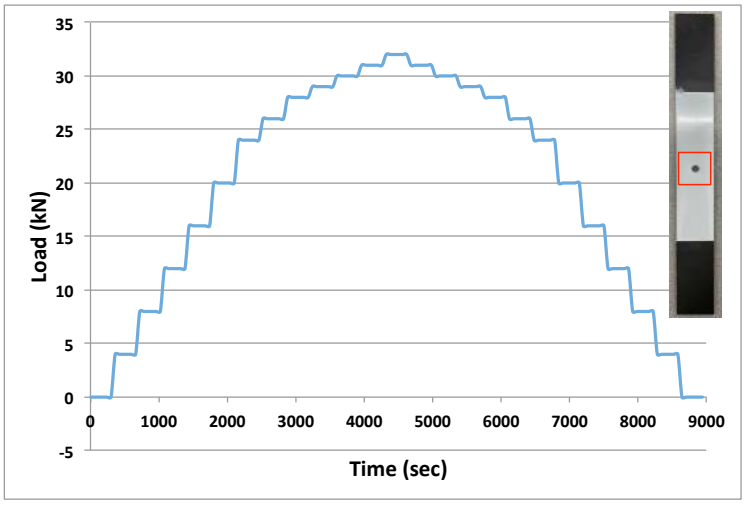

Figure 4.2: Load step plot for tensile testing of the OHT CFRP sample with paint-based PS coating. An image of the OHT CFRP sample is shown on the right with the mapped region boxed in red.

Table 4.1: Mechanical, PS and DIC parameters that were used for tensile testing of the notched Al-2024 and OHT CFRP samples with paint-based PS coating.

Mechanical Test Parameters		
	Al-2024	OHT CFRP
Displacement rate	0.2 mm/min	
Grip pressure	11 MPa	
Maximum load	24 kN	32 kN
PS Data Collection Parameters		
	Al-2024	OHT CFRP
Laser power	15 mW	
Exposure time	25 ms	40 ms
Number of exposures per frame	1	
Resolution	400 μm	
Map size	42.4 mm $\times$ 25.6 mm	25.6 mm $\times$ 25.6 mm
Pixel map size	106 points $\times$ 64 points	64 points $\times$ 64 points
DIC Data Collection Parameters		
	Al-2024	OHT CFRP
Image capture rate	1 image/sec	
Framerate	15 fps	
Bin size	1 $\times$ 1	
Resolution	3500 $\times$ 3500	

4.3 Paint-Based Piezospectroscopic Coating Stress Sensing on a Notched Aluminum Specimen

The PS and DIC maps were compared side-by-side, as shown in Figure 4.3. The DIC maps exhibit increasing tensile strain and larger strains concentrated at the notch with increasing load, which was the expected trend. On the other hand, the PS maps exhibited leftward peak shifts with increasing load. The paint-based PS coating did not sense stresses near the notch while the DIC maps captured higher strains in that area. The peaks shifted left from the zero load, which suggests that the particles in the coating may be experiencing stress relaxation. It is possible that damage, particularly microcracks, in the coating occurred during the load tests, causing the coating to experience stress relaxation. Another reason for the opposite peak shift trend could be that the particles are not well adhered to the polymer matrix, which would cause the load not to transfer from the polymer to the particles. Changes in temperature could also have an effect on the peak shifts. These hypotheses are further investigated in this chapter.

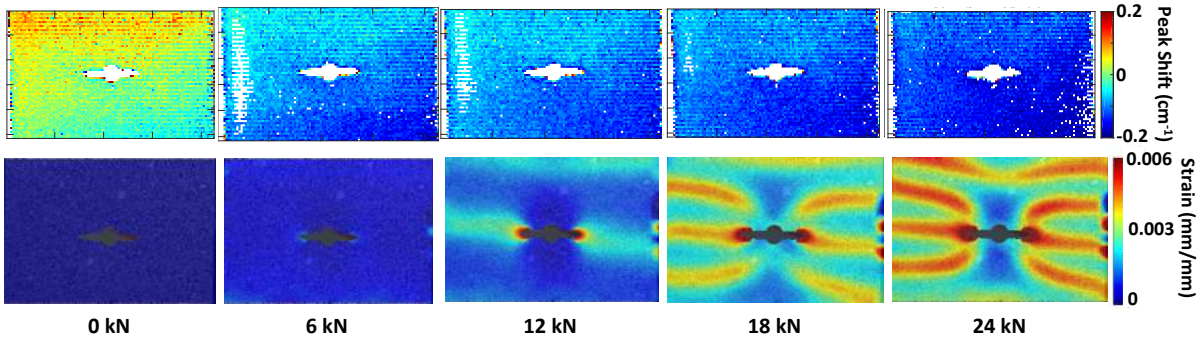

Figure 4.3: PS (top row) and DIC (bottom row) contour plots showing change in peak shift and strain, respectively, with increasing load. For the peak shift maps, the data points are with reference to their local zero load peak position.

Although the shift does not follow the expected rightward shift, the sensitivity of the paint-based PS coating on the notched Al-2024 substrate was quantitatively assessed by plotting the R1 peak shifts with respect to the tensile stress, as shown in Figure 4.4. A nonlinear trend can be seen in the plot. Between 0.05 GPa and 0.15 GPa, the peak shift is very sensitive to load, but then this sensitivity decreases when the load exceeds 0.15 GPa. It can be implied that micro-damage within the paint-based PS coating was occurring rather than detachment of the coating from the substrate. Thus, when the coated OHT CFRP sample was tested, the peak shifts during unloading of this samples was also monitored to confirm that micro-damage was occurring.

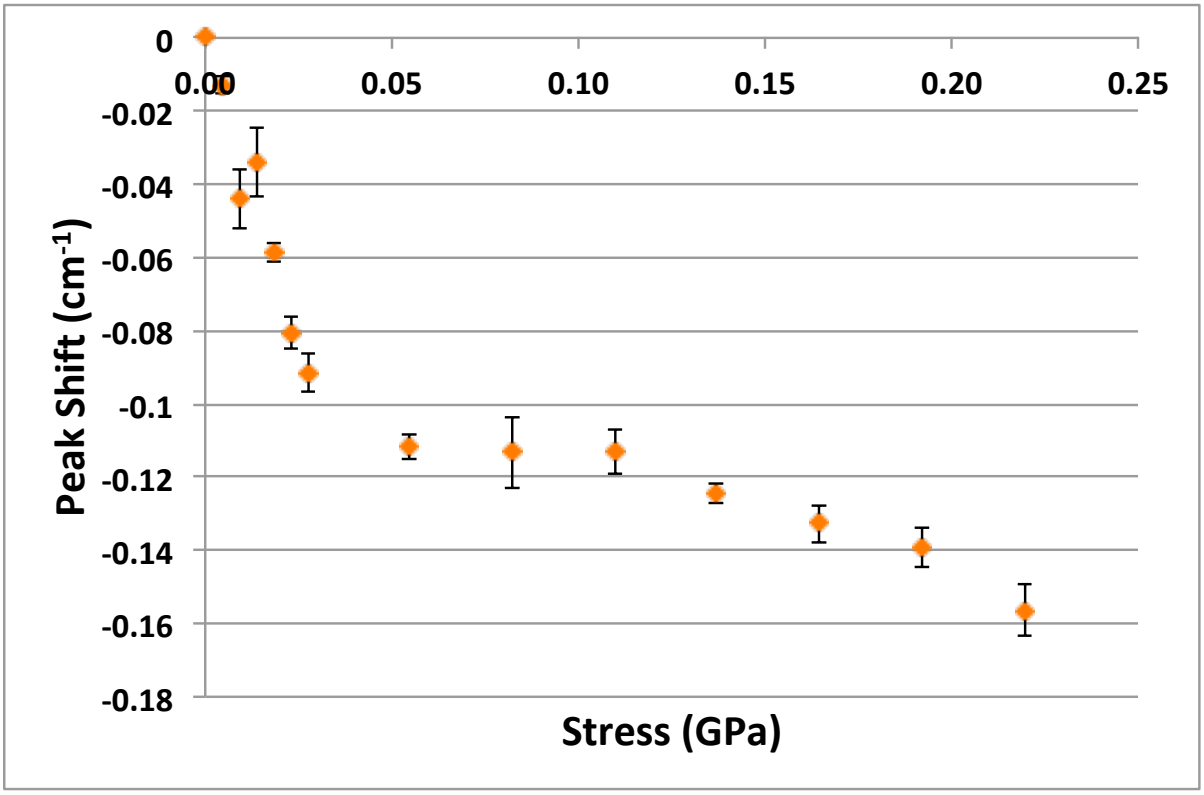

Figure 4.4: Peak shift of the R1 peak vs. stress for the paint-based PS coating on a notched Al-2024 substrate. The error bars are based on the standard error of four peak shift averages taken from four regions of each PS map.

4.4 Paint-Based Piezospectroscopic Coating Stress Sensing on an Open-Hole Tension Composite Specimen

PS and DIC maps were obtained during the loading and unloading of the coated OHT CFRP sample, as shown in Figure 4.5. The DIC maps show strains that are reflective of the loading

conditions of the OHT CFRP substrate. Strains increased as the substrate was loaded up to 32 kN and decreased as the substrate was unloaded. However, the PS maps show that, during loading and unloading of the sample, the R1 peaks continually shift leftward, which is different from the expected trend for tensile loading. Also, in the unstressed state, the pre-load and post-load peak shift maps are not the same. Similar to the paint-based PS coating on the Al-2024 substrate, the paint-based PS coating did not sense the stress state of the OHT CFRP substrate at either the surface and subsurface level, whereas the DIC maps reflected higher strains in the $\pm 45^{\circ}$ plies. Although the PS shifts were uncharacteristically suggesting relaxation of stress in the particles with tensile loading, the sensitivity of the paint-based PS coating on the OHT CFRP substrate was assessed by plotting the R1 peak shifts with respect to the applied stress, as shown in Figure 4.6. Like the peak shift versus stress plot for the notched Al-2024 sample 4.4, the trends of the plots in the loading and unloading conditions are nonlinear. It can be seen from Figure 4.6 that the R1 peak shift drops down to approximately -0.40 cm^{-1} at post load from the unstressed state, which further confirms the shifts observed in the peak shift maps (Figure 4.5).

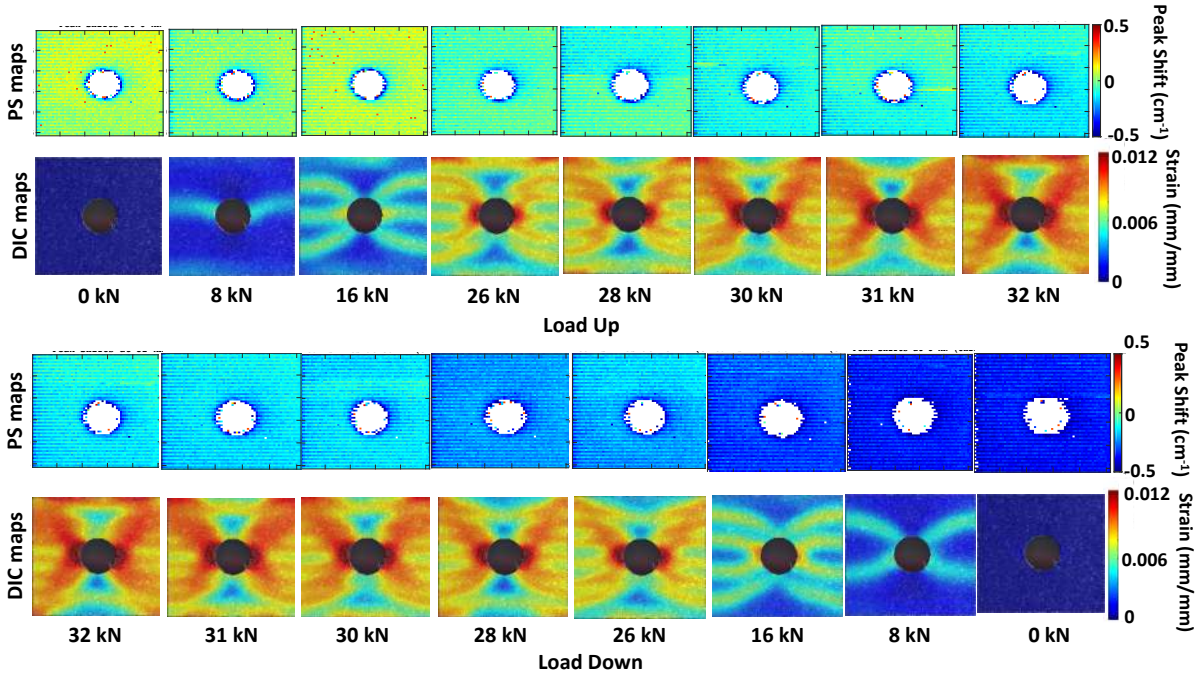

Figure 4.5: PS and DIC maps showing the progression of peak shift and strain, respectively for loading and unloading of the OHT CFRP sample with paint-based PS coating.

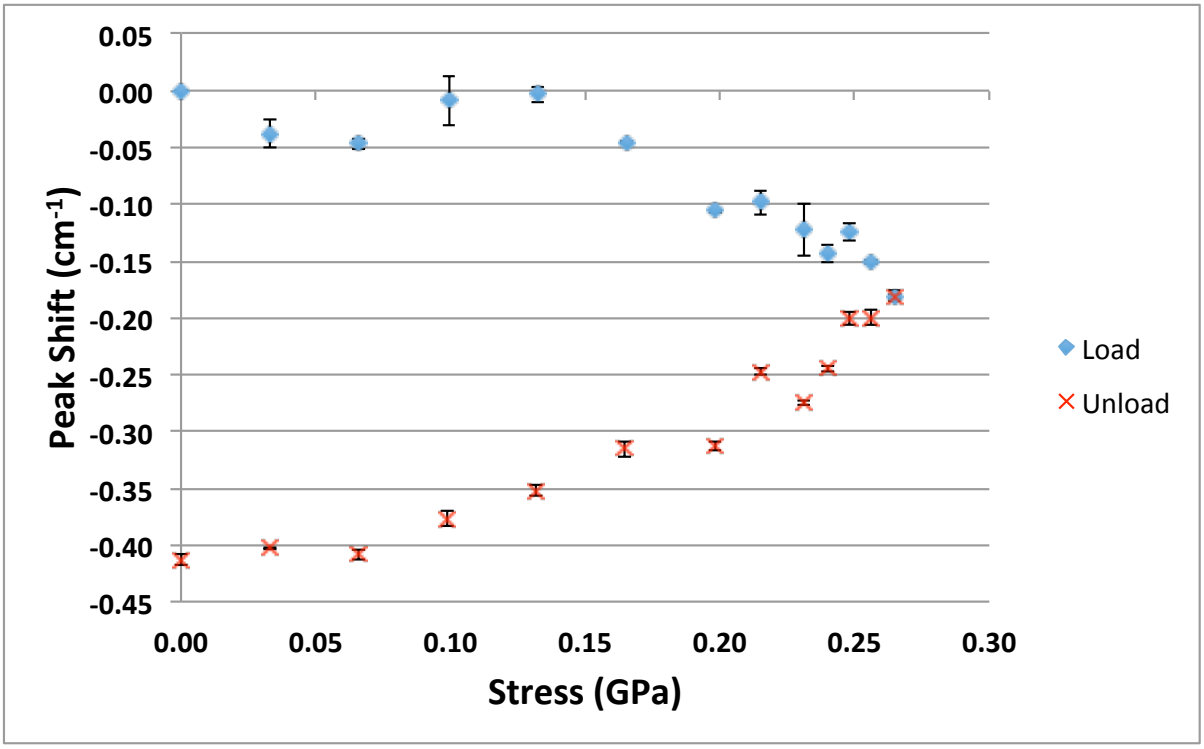

Figure 4.6: Peak shift of the R1 peak vs. stress for the paint-based PS coating on an OHT CFRP substrate. The error bars are based on the standard error of four peak shift averages taken from four regions of each PS map.

Based on the results of the tests done on the notched Al-2024 and OHT CFRP substrates with paint-based PS coating, it was shown that the paint-based PS coating responds with left-ward R1 peak shifts with increasing tensile load and does not correlate with the stress and strain concentrations at the notch or hole from DIC. Since the coating at post load exhibited greater leftward shifts from the unstressed state, it was suspected that micro-damage of the nanocomposite coating might have occurred during the load tests. In the next section, the scan-

ning electron microscopy (SEM) images of the coating before and after load were assessed for signs of damage.

4.5 Inspection of the Paint-Based Piezospectroscopic Coating Using Scanning Electron Microscopy

It has been observed from all of the load tests that the peak shifts did not correlate with the applied tensile load, which could be attributed to micro-damage happening within the paint-based PS coating that could not be visually observed. To confirm this, SEM was done on the coating before and after load tests to determine whether damage occurred due to manufacturing or applied load. A sample with the paint-based PS coating that has not been subjected to load tests was inspected using SEM to look for signs of manufacturing defects. Some pores were spotted on the surface and cross-section of the coating, which could have contributed to the formation of cracks during load tests. Images of these pores are shown in Figure 4.7.

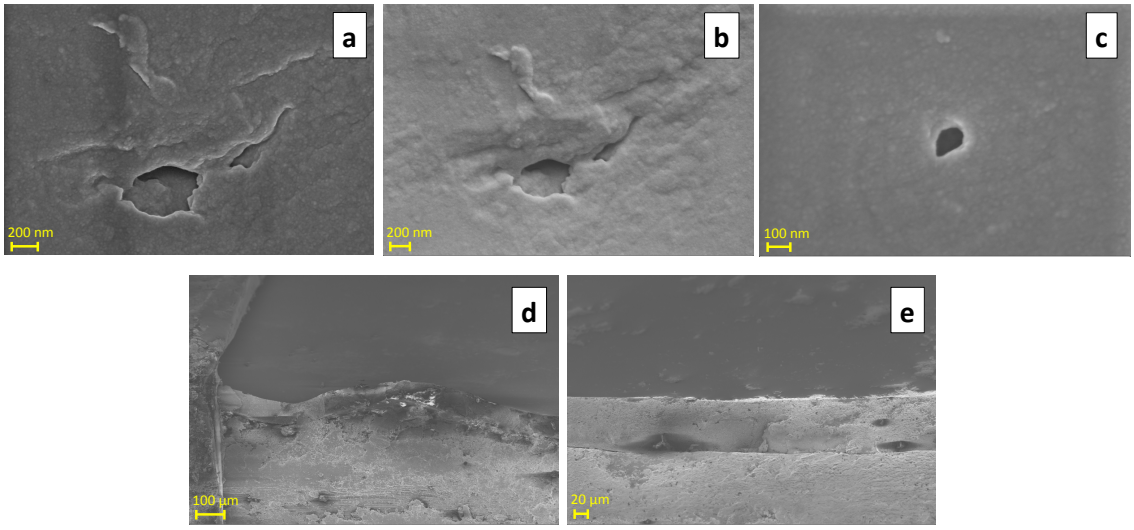

Figure 4.7: The SEM images shown here were taken from a sample with paint-based PS coating that was not subjected to load tests. Pores were found on the surface (a, b and c) as well as the cross section of the coating (d and e).

Signs of micro-damage were seen in the SEM images after the paint-based PS coating was subjected to load (Figure 4.8). Microcracks and additional pores were found in the coating, which confirmed that micro-damage had happened during the load tests. Areas of agglomerations and uneven surfaces were spotted as well, though they might have existed due to manufacturing. Image f in Figure 4.8 provides a closer look into one of the microcracks, which reveals a granular structure within the paint. It is possible that the cracks not only resulted from pores, but also due to the particles and matrix not being well adhered to each other.

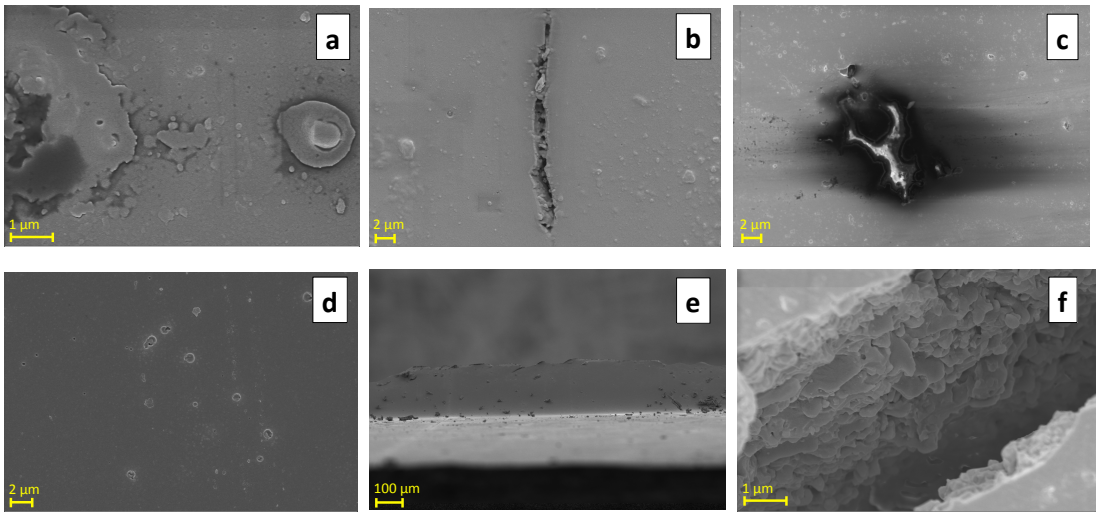

Figure 4.8: The SEM images taken after load tests indicate microcracks (a and b), agglomerations (c and d), pores (d) and uneven surface (e). The inside of one of the microcracks (f) reveals a granular structure within the paint-based PS coating.

4.6 Temperature Effect on the Paint-Based Piezospectroscopic Coating

Thus far, the peak shifts were assessed with respect to stress. However, it is also known that R-lines shift with increasing temperature [69, 70]. He and Clarke [39] performed a temperature calibration to ensure consistent calibration for the ruby specimen that was tested. Although their tests were performed at room temperature and sufficiently low laser powers were used,

temperature was monitored during their tests, and peak shift correction was applied for any room temperature changes. For the case of a polymer ceramic material, Stevenson et al [45] performed a temperature calibration test that demonstrated that the effects of temperature are negligible since the empirically obtained PS coefficients were much smaller than those obtained from stress-induced peak shifts.

In this work, the paint-based PS coating, a polymer ceramic material, was tested to determine the temperature effect on the R1 peak shift. A PS map scan of a paint-based PS coating sample that was not subjected to load was taken at room temperature using map dimensions of 12.8 mm $\times$ 4.8 mm. Heat was then applied to this sample, and an infrared camera was used to measure the temperature of the coating. PS map scans were taken at 35.8°C and 38.5°C using the same map dimensions. Afterwards, another map scan of the sample was taken when it cooled down to 32°C. Figure 4.9 shows the resulting R1 peak shift maps with respect to temperature change.

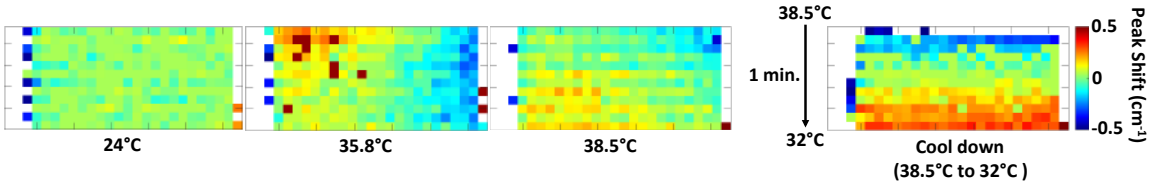

Figure 4.9: Peak shift maps showing changes in peak position with increasing (room temperature (24°C) to 38.5°C) and decreasing (38.5°C to 32°C) temperature from the unstressed state.

It was observed from the PS maps that the R1 peaks shifted from the unstressed state at temperatures 35.8°C and 38.5°C. As the paint-based PS coating sample was cooled down from 38.5°C to 32°C, a map scan, in a snake-like pattern, was taken in one minute, starting from the top left corner to the bottom right corner of the area of interest. The resulting map revealed a gradient of peak shifts during cool down, and the shifts were changing at a rate of 0.154 cm^{-1}/°C. This indicates the possibility that the paint-based PS coating is sensitive to temperature change. However, considering that the sample was subjected to high temperatures, it can be inferred that a significant amount of heat would cause discernible leftward peak shifts. For this work, the temperature effect on peak shift was quantified and compared to literature. It was assumed that, during the dispersion and load tests, that temperature variations in the testing room were low enough to not cause a significant effect on peak shift measurements. Future tests need temperature monitoring to ensure that this assumption is valid.

4.7 Assessment of the Polymer Matrix

It has been shown in previous work that PS coatings made with α-alumina nanoparticles in epoxy resin were sensitive to changes in the stress state of the underlying substrate. The type of polymer used in the coating has an effect on the load transfer from polymer to particle. The polyurethane matrix used in this work is similar to the epoxy resin in that they are both two-part, thermosetting matrix systems. However, the paint-based PS coating's and the alumina-epoxy PS coating's sensing capability could be affected by their mechanical properties. A study by

McBride et al [71] used a bisphenol A/epichlorohydrin derived liquid epoxy resin, which is the same type of epoxy resin used in the alumina-epoxy PS coatings. The study showed that the epoxy resin has an elastic modulus of 2.56 GPa and an ultimate tensile strength of 56.9 MPa. In another study by Sabzi et al [72], it was found that the polyurethane clear topcoat has an elastic modulus of 350 MPa and an ultimate tensile strength of 9.76 MPa. It is evident that polyurethane has a lower tensile strength compared to the epoxy resin. Further studies to assess the stress sensitivity of the paint-based PS coating can provide more information on its mechanical response. Future iterations of the paint-based PS coating will consider the mechanical properties of the polymer matrix to improve particle bonding and mechanical response. The differences in material properties could have had an effect on the bonding between the alumina particles and polymer matrix. Prior to curing, the epoxy resin is a viscous liquid and has a relative density of 1.17 [73], whereas the polyurethane clear topcoat is a liquid with a relative density of 0.91 [74]. It is possible that a more viscous liquid with higher relative density is needed to ensure a stronger bond between the particles and matrix after curing.

4.8 Summary of Results

The results of this chapter further confirmed the trends shown in Chapter 3 in which the paint-based PS coating exhibited peak shift trends that do not correlate with tensile load, but rather suggest stress relaxation of the coating. Additionally, the coating was not able to sense the stress state of the metallic and composite substrates at the surface and subsurface level, whereas

the DIC results showed higher strains near the notch of the Al-2024 substrate and the hole of the OHT CFRP substrate. Inspection of the paint-based PS coating before and after load using SEM confirmed that micro-damage occurred during load tests as a result of manufacturing defects, namely porosity and poor particle and matrix interaction. This implies that the bond between the polymer matrix and alumina nanoparticles may be weaker than the previous matrix used (epoxy resin) and initial manufacturing defects, such as pores, contribute to the non-characteristic leftward shift, which is non-recoverable upon unloading. Possibly a more compatible matrix, would need to be considered for future iterations to ensure that the particles and matrix are well adhered to each other. Results of the temperature effect test show that temperature effects should be monitored to effectively substantiate that the impact is negligible.

CHAPTER 5
CALIBRATION OF THE PHOTOLUMINESCENCE HYPERSPECTRAL IMAGER

5.1 Instrumentation Background, Motivation and Requirements

In previous work, a portable PS system was developed to allow for in-situ spectral measurements, thereby increasing the functionality and adaptability of this technique in industry [75]. Though this system can generate high spatial resolution maps, the process of collecting data point-by-point while maintaining high resolution is time consuming. In this work, the photoluminescence hyperspectral imager (PHI) system was conceived as an innovative solution that can capture the PL spectra of a material over an area of a structure. It uses the data collection principle of hyperspectral imaging, which is an emerging technique and can be applied to PL measurements. It has applications in agriculture, medicinal science, and hazardous material detection [12, 13, 14]. The advantage of hyperspectral imaging is that it collects, at each pixel, a cube of data in a short amount of time to produce images. This data cube consists of a set of x and y physical images for linear wavelength increments in the z-direction and can utilize a range of wavelengths from visible to short wave infrared (i.e. from 400 nm to 2500 nm) in one pixel [76]. Pixels can then be characterized by the spectral "fingerprint" reflected based on the molecular composition of the material with resolution in nanometers [14, 76]. For the purposes of this PHI system, a tunable filter is used to set the region of interest to 680 - 697 nm, which correlates to 14,347.2 - 14,705.6 cm^{-1} as this represents the spectral region of interest to capture R-lines from α-alumina. A concept for photoluminescence measurements used in conjunction with the PHI for stress sensing is represented by a schematic in Figure 5.1.

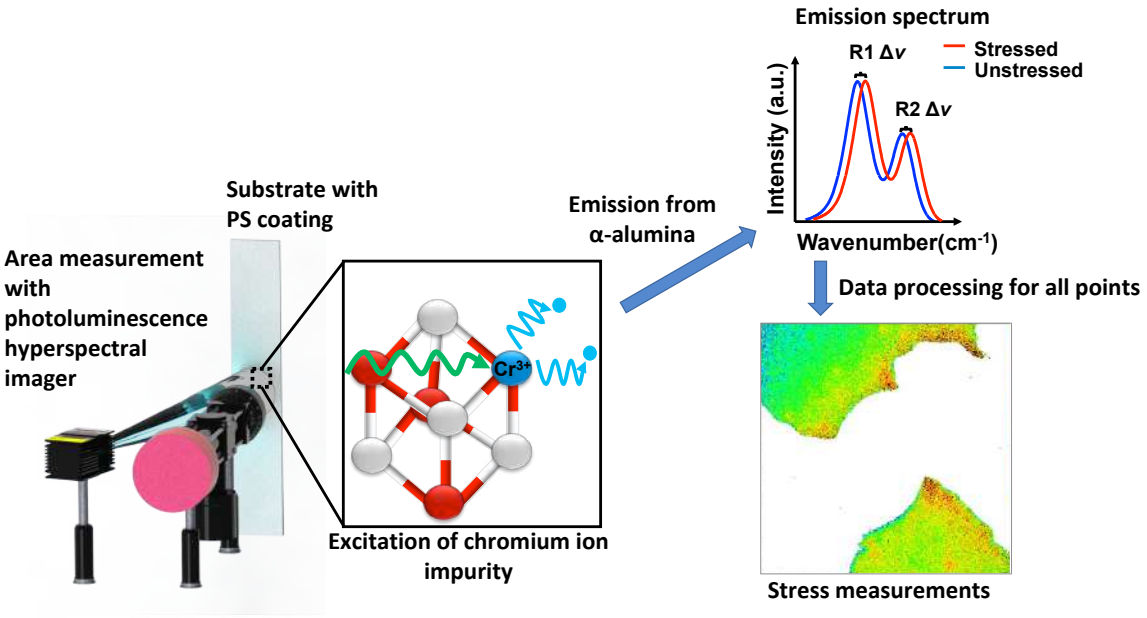

Figure 5.1: Targeted application for next generation stress sensing using the area measuring capability of the photoluminescence hyperspectral imager.

In order to be of practical use in industry as an NDE technique, it is imperative that the instrument should perform stress and damage sensing efficiently while having multi-scale spatial resolution and high stress resolution. Thus, the PHI was designed to optimize the PL measurement technique. For this work, the PHI was required to meet certain benchmark capabilities when compared to the portable PS system previously developed. The PHI must surpass the portable PS system in terms of surface scanning and data acquisition time. Specifically, it should be able to measure an area of a surface rather than taking point-by-point scans and achieve shorter data acquisition time than the portable PS system. Along with these char-

acteristics, the PHI must be able to characterize the PS coatings' particle dispersion via PL spectroscopy and perform stress and damage sensing via PS. These capabilities would elevate this technique and its application in an operational context for aircraft structures.

5.2 Description of the Photoluminescence Hyperspectral Imager

5.2.1 Overview of the Hardware Components and Instrument Set Up

The PHI is composed of hardware components that are required for obtaining photoluminescent maps (Figure 5.2). This section describes the components and their functionalities and how they contribute to data collection. The mercury-neon (HgNe) and argon (Ar) lamps are used to perform wavelength calibration based on the reference emission lines at 690.752 nm (mercury (Hg)) and 696.543 nm (argon (Ar)) [77]. Once the PHI is calibrated, it enables measurement of R-lines with an accuracy of 0.01 nm. To excite the chromium ions in the α-alumina particles present in the PS coating, a 445 nm laser diode is used. It is a high-powered laser with a maximum output power of 2.5 W. The output laser spot is elliptical in shape. The beam focus can be adjusted until the area of interest on a test specimen surface is fully illuminated. A variable DC power supply unit controls the laser output power. The maximum electrical output is 9 W. Generally, the peak optical power is 7.8 W, and the threshold for initiation of the laser beam is at 1.6 W.

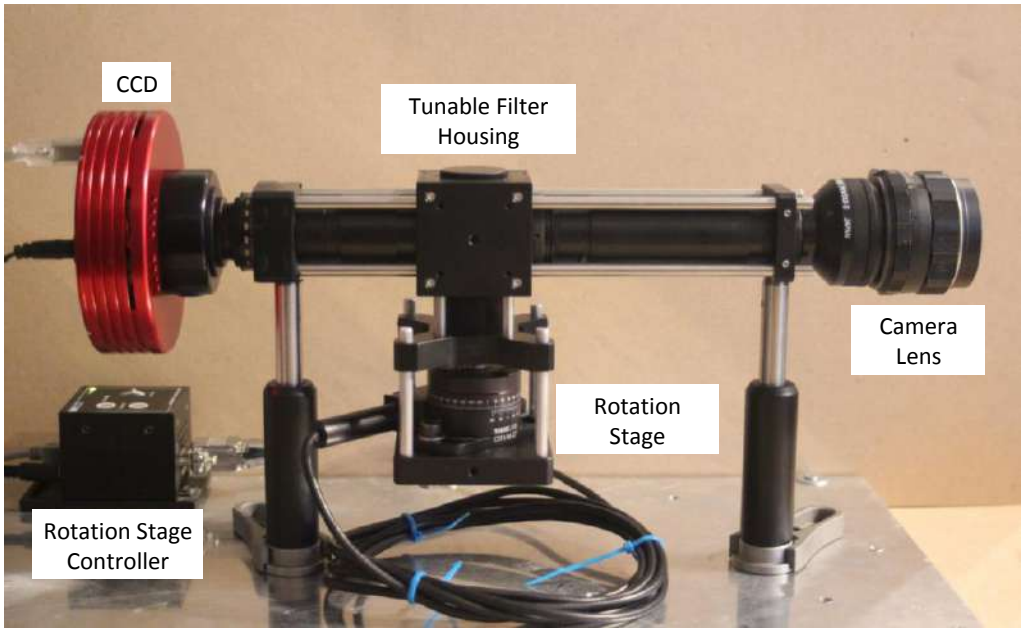

Figure 5.2: The photoluminescence hyperspectral imager and and its major components.

The PHI consists of a tunable narrow bandpass dielectric filter, which transmits light in the range of 680 nm to 697 nm with a bandpass of 0.1 nm full width half maximum (FWHM) (Omega Optical Inc., VT) [77]. This range is specific to the needs of the application. In this case, the filter meets the needs for detection of the α-alumina R-lines. The center wavelength of transmission is dependent on the angle of incidence of the filter. To tune the center wavelength, a controlled, motorized rotation stage is used to tilt the filter with high precision. This rotation stage (Thorlabs, Inc.) has a step size of 0.1°. At each angle of incidence, from 7° to 14°, an image of the area of interest of the test specimen surface is taken. By collecting images at various angles, a data cube is acquired, which provides the spectral points needed to construct

the R-lines. This approach allows the user to control the spectral resolution. Figure 5.3 shows how data is collected using the tunable filter.

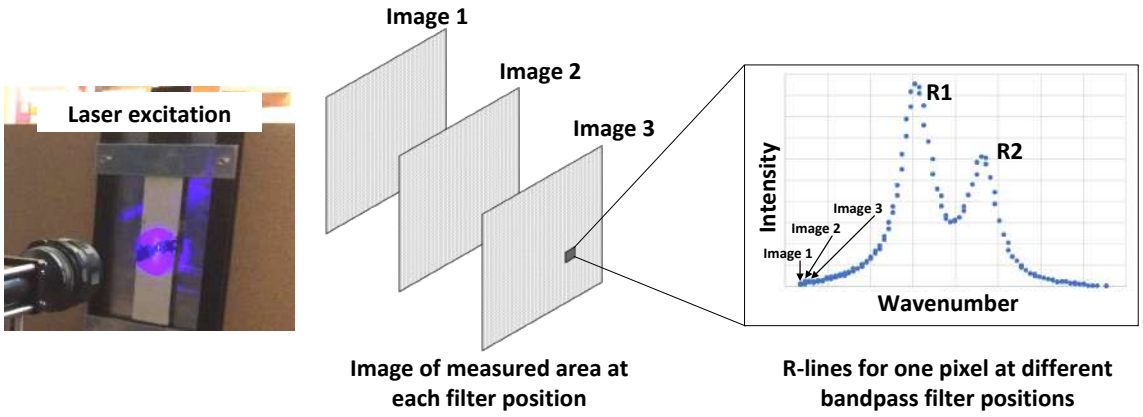

Figure 5.3: Schematic of data acquisition via laser excitation of the PS coating and image capture at each filter position.

The image of the luminescent test specimen is focused with a camera lens that has an f/3.5 aperture, which is located at the front of the PHI system, followed by two additional lenses. The standard standoff distance from the front of the lens to the test specimen's PS coated surface is 18 cm for optimum image quality. The tunable bandpass filter and rejection filter are located within the PHI system, which are set in this application for transmitting optical signal in the 694 $\pm$ 5 nm range of interest for α-alumina and rejecting background light and laser irradiation. The CCD is a low noise camera that acquires the focused image of a luminescent test specimen. It has a resolution of 1391 pixels $\times$ 1039 pixels and a pixel size of 6.45 μm $\times$

6.45 μm. Data acquisition and analysis is achieved with the PHI system's software, which is discussed further in Section 5.2.2.

5.2.2 Overview of Software for Spectral Data Acquisition and Analysis

The PHI system utilizes Thorlabs APT, Artemis Capture, and National Instruments (NI) LabVIEW for controlling the rotation stage, gathering data from the CCD camera, and processing and analyzing data, respectively. LabVIEW performs four steps: data acquisition, raw data viewing and reshaping, data fitting, and contour map plotting. To perform data acquisition, the user inputs parameters for taking spectral measurements, including the filter angle range (7° to 14°), filter angle step size (at least 0.1°), number of images, and exposure time (varies with photoluminescence signal quality). Once these parameters are inputted into LabVIEW, the total amount of time to acquire the raw data from the luminescent test specimen is given. As the software acquires the data, the user can view the remaining data acquisition time and images to take and the filter's current position. After the raw data is obtained, a reshaped data cube is generated and stored as a separate file. In this step, data with high noise and low intensity is filtered out of the raw data, which results in a reshaped data cube with low noise data. The third step of the analysis is to perform data fitting with the reshaped data cube, which utilizes the nonlinear least squares fitting method to plot the R-lines. The accuracy of the R-line peak position is dependent on the SNR of the data and the number of points collected. Using the regularized inversion method, the measured spectral emission is reconstructed to provide ac-

curate R-line peak values in the order of 0.01 nm. The user inputs the parameters for fitting, including bin size, step size, map size based on the number of pixels in the x- and y-directions and threshold for peak fitting. The reference wavelength can also be indicated in the software, which includes Hg (690.752 nm), Ne (692.989 nm), Ar (696.543 nm), α-alumina in thermal barrier coatings (694.403 nm) and R1 for sapphire (694.348 nm) as references. As the software is running, the user can view the percentage of fitting that is completed and preview the peak shift and intensity (particle dispersion) maps. For the fourth step, the fitted data is plotted to obtain the finalized intensity and peak shift contour maps.

5.3 Validation Tests on Composite and Metallic Specimens for Measuring Piezospectroscopic Coating Intensity and Peak Shift

Two specimens were tested using the PHI system and were compared to tests using the PS system. One test specimen was an OHT CFRP specimen coated with 20 vol% of 150-nm sized α-alumina particles in epoxy matrix, as described in Chapter 2, Section 2.2. Another test specimen was a tensile aluminum specimen coated with 10 vol% of 150-nm sized α-alumina particles in epoxy matrix and with a notch on the opposite side of the coated surface, as described in Chapter 2, Section 2.3. Both specimens were taken to failure prior to these experiments.

An area of 14 mm $\times$ 14 mm on the OHT CFRP specimen, with the hole at the center, was chosen as the area of interest for testing. Table 5.1 shows the data acquisition parameters that

were used to obtain spectral data from this specimen. The resolution, physical map size and spectral map size were kept consistent when using the PHI and PS systems.

Table 5.1: Test parameters for the OHT CFRP specimen with PS coating consisting of 20 vol% α-alumina for both measurement systems.

Test Parameters	**PS System**	**PHI System**
Laser power (mW)	7.1	1000
Exposure time (ms)	1	40,000
Physical map size (mm^2)	14×14	14×14
Pixel map size	350×350	350×350
Spatial resolution (μm)	40	40
Number of images	1	80
Total scan time (minutes)	63	53

The PHI performed the map scan in 16 % less time than the PS system. To further assess the capabilities of the PHI, the intensity and peak shift maps from the PS and PHI systems were compared. Figure 5.4 show a comparison of intensity maps that characterize the dispersion of the α-alumina particles and peak shift maps that represent the stress state of the PS coating.

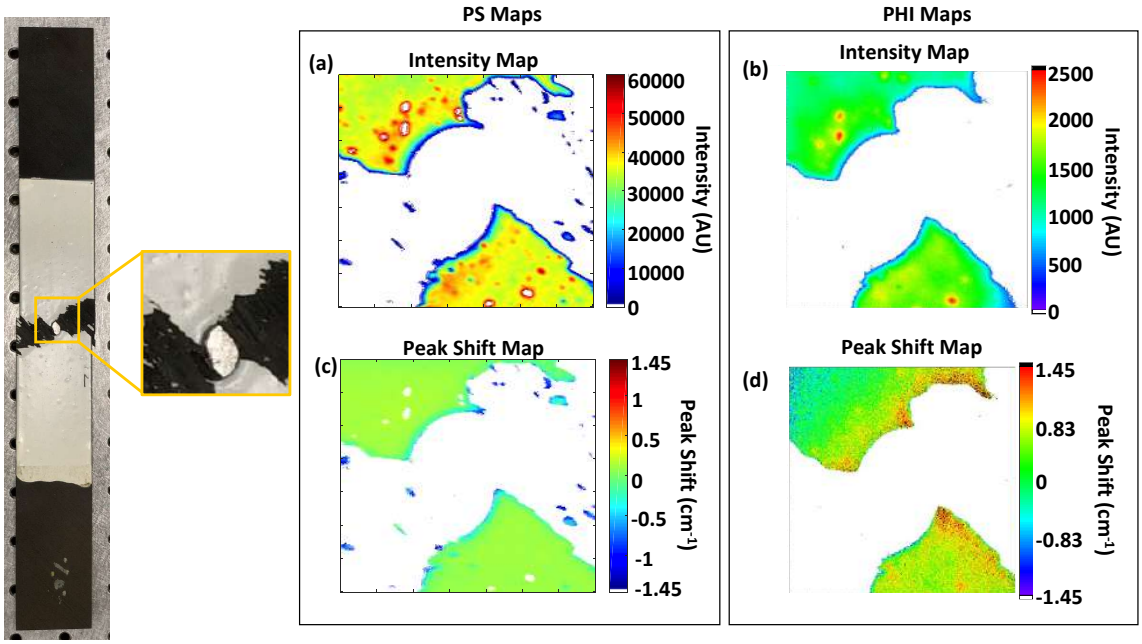

Figure 5.4: Close-up view of the mapped area on the OHT CFRP specimen with PS coating consisting of 20 vol% α-alumina in PS coating with comparisons of dispersion maps from the (a) PS system and (b) PHI; and peak shift maps from the (c) PS system and (d) PHI system. Each map is 14 mm $\times$ 14 mm.

An area of 16.8 mm $\times$ 28.8 mm on the aluminum tensile specimen with 10 vol% α-alumina in PS coating, with the notch at the center, was chosen as the area of interest for testing. Table 5.2 shows the data acquisition parameters that were used to obtain spectral data from this specimen. The resolution, physical map size and spectral map size were kept consistent.

Table 5.2: Test parameters for the aluminum tensile specimen with PS coating consisting of 10 vol% α-alumina for both measurement systems.

Test Parameters	**PS System**	**PHI**
Laser power (mW)	10.6	1000
Exposure time (ms)	20	10,000
Physical map size (mm^2)	16.8×28.8	16.8×28.8
Pixel map size	140×240	140×240
Spatial resolution (μm)	120	120
Number of images	1	80
Total scan time (minutes)	26	13

Due to the lower α-alumina particle content in the aluminum specimen's PS coating in comparison to the 20 vol% of α-alumina in the OHT CFRP specimen's PS coating, the resolution was increased from 40 μm to 120 μm on both the PS and PHI systems. The PHI performed the map scan in 50 % less time than the PS system. To further assess the capabilities of the PHI, the intensity and peak shift maps from the PS and PHI systems were compared. Figure 5.5 shows the comparison of the intensity maps and the peak shifts.

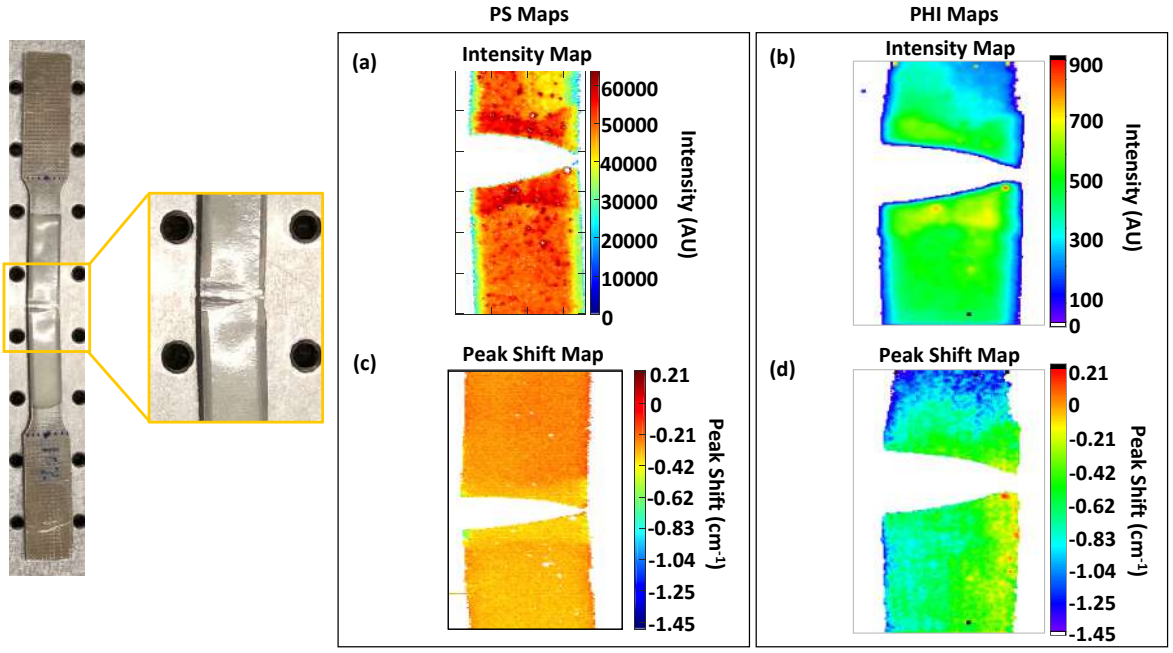

Figure 5.5: Close-up view of the mapped area on the aluminum tensile specimen with PS coating consisting of 10 vol% α-alumina in PS coating with comparisons of dispersion maps from the (a) PS system and (b) PHI; and peak shift maps from the (c) PS system and (d) PHI system. Each map is 16.8 mm $\times$ 28.8 mm.

Comparing the PS and PHI intensity map in Figures 5.4 and 5.5, the PHI intensity map showed discernible features that reveal variations in particle dispersion within the PS coating within a smaller range of intensities than the PS intensity map. The lower intensity readings from the PHI is due to attenuation caused by dispersing the beam of the laser excitation source, which is necessary to achieve area measurement. A high optical laser power is used, as mentioned in Section 5.2.1, to compensate for this attenuation. Despite the low intensity readings,

the measurements are adequate enough to characterize particle dispersion in PS coatings. The residual peak shifts were more noticeable in the PHI maps than in the PS maps within the peak shift range used for these maps. This result is attributed to the differences in spectral resolution between the two measurement systems. The peak wavelength accuracy, or spectral resolution, of the PHI is 0.01 nm, or 0.2 cm^{-1} [78]. This resolution is 0.18 cm^{-1} smaller than that of the PS system, which is 0.38 cm^{-1} (0.02 nm).

5.4 Summary

The PHI was designed to provide area measurement and fast data acquisition time with acceptable spectral resolution for stress sensing. To achieve area measurement, the PHI utilizes a laser excitation source with an adjustable aperture, so that the user can widen or narrow the aperture as desired to illuminate to area of interest on a test specimen. As the beam of the laser excitation source is widened, attenuation is increased, resulting in lower intensity readings. To compensate for the attenuation, a high optical laser power is used. Data acquisition time was reduced, using the PHI, by 16 % when measuring the OHT CFRP specimen with 20 vol% α-alumina in PS coating and by 50 % when measuring the aluminum tensile specimen with 10 vol% α-alumina in PS coating. It can be seen that the PHI achieved area measurement and reduction in data acquisition time.

CHAPTER 6
CONCLUSIONS

In this work, the processing approach used for the paint-based PS coating and its impact on particle dispersion and mechanical response were investigated through piezospectroscopy. Based on the dispersion maps and histograms, it was found that adding the coating components into the mixture in the following order - base component, dispersant alumina nanoparticles, and activator - and using a coating thickness of 5 mil improved dispersion while demonstrating a response to applied stress.

Spectral measurements obtained through piezospectroscopy showed leftward peak shifts with increasing tensile load, which is contradictory to the trend observed in previous studies with an alumina-epoxy PS coating where rightward shifts corresponded to increasing tensile load. This opposite trend in peak shifts suggest that the alumina nanoparticles within the coating were experiencing stress relaxation. The peak shift versus stress plot for the notched Al-2024 sample with the paint-based PS coating shows a nonlinear trend in the data indicating the possibility of coating micro-damage occurring during load tests or weak particle-to-polymer bonding. Loading and unloading of the OHT CFRP sample with paint-based PS coating showed that the stress within the coating is non-recoverable, which further confirmed that micro-damage or weak particle-to-polymer bonding was possibly occurring. SEM images taken from an unloaded sample with paint-based PS coating revealed areas with pores. These pores may have contributed to the formation of microcracks, as seen in the SEM images taken from a sample that was subjected to load. These results, thus, confirmed that the paint-based

PS coating was sensing stress relaxation due to microcracking within the coating. There is a possibility that the paint-based PS coating is sensitive to changes in temperature since shifts in the R1 peaks were observed from the temperature effect test.

Previous work on alumina-epoxy PS coatings have demonstrated high sensitivity to stress and ability to detect subsurface damage. A comparison of mechanical and material properties between the epoxy resin and polyurethane clear topcoat showed that the polyurethane clear topcoat is not as ideal as epoxy resin for strong particle-to-polymer bonding. Future work will consider using a polymer matrix that has similar mechanical properties as epoxy resin while being applicable to aircraft structures. PS coatings made with varying polymer matrix systems will be tested for their stress and damage sensing capability. Another factor that will be considered and improved on are the particle-to-polymer bonding. Variation in particle size and volume fraction will also be considered in tuning the polymer properties, which may provide more sensitivity to stress.

The PHI had demonstrated capability in area measurement and faster data collection time, which are desirable characteristics for use as an NDE instrument. Future work will focus on its capability in measuring peak shifts with applied load during mechanical tests and on portability of this instrument for on-the-go NDE.

LIST OF REFERENCES

[1] G. Freihofer, J. Dustin, H. Tat, A. Schülzgen, and S. Raghavan, "Stress and structural damage sensing piezospectroscopic coatings validated with digital image correlation," *AIP Advances*, vol. 5, no. 3, p. 37139, 2015.

[2] I. Hanhan, A. Selimov, D. Carolan, A. C. Taylor, and S. Raghavan, "Quantifying Alumina Nanoparticle Dispersion in Hybrid Carbon Fiber Composites Using Photoluminescent Spectroscopy," *Applied Spectroscopy*, vol. 71, no. 2, pp. 258–266, 2017.

[3] G. Riegert, K. Pfleiderer, H. Gerhard, I. Solodov, and G. Busse, "Modern methods of NDT for inspection of aerospace structures," *ECNDT, Berlin, Germany*, 2006.

[4] V. Giurgiutiu, J. M. Redmond, D. P. Roach, and K. Rackow, "Active sensors for health monitoring of aging aerospace structures," in *PROCEEDINGS-SPIE THE INTERNATIONAL SOCIETY FOR OPTICAL ENGINEERING*. International Society for Optical Engineering; 1999, 2000, pp. 294–305.

[5] Y.-K. Zhu, G.-Y. Tian, R.-S. Lu, and H. Zhang, "A review of optical NDT technologies," *Sensors*, vol. 11, no. 8, pp. 7773–7798, 2011.

[6] M. Dresselhaus, G. Dresselhaus, A. Jorio, A. Souza Filho, and R. Saito, *Carbon*, vol. 40, no. 12, pp. 2043–2061, 2002.

[7] A. Merlen, N. Bendiab, P. Toulemonde, A. Aouizerat, A. San Miguel, J.-L. Sauvajol, G. Montagnac, H. Cardon, and P. Petit, "Resonant Raman spectroscopy of single-wall carbon nanotubes under pressure," *Physical Review B*, vol. 72, no. 3, p. 035409, 2005.

[8] M. Dresselhaus, G. Dresselhaus, R. Saito, and A. Jorio, "Raman spectroscopy of carbon nanotubes," *Contemporary Concepts of Condensed Matter Science*, vol. 3, pp. 83–108, 2008.

[9] G. Freihofer, L. Poliah, K. Walker, and S. Raghavan, "Optical stress probe: in-situ stress mapping with Raman and photo-stimulated luminescence spectroscopy," *Journal of Instrumentation*, vol. 5, p. P12003, 2010. [Online]. Available: https://storage.cecs.ucf.edu//Groups/MMAE-Seetha/ALOX/StudentPapersandConferences/PortableSpectroscopyPaper/Imad/Literature/ExampleJINSTpapers/OpticalStressProbe.pdf

[10] G. J. Freihofer, "Enhancing CNT-Composites with Raman Spectroscopy," Master's thesis, 2011.

[11] G. Freihofer, F. Liang, B. Mohan, J. Gou, and S. Raghavan, "Ex-situ Raman spectroscopy to optimize the manufacturing process for a structural MWNT nanocomposite," *International Journal of Smart and Nano Materials*, vol. 3, no. 4, pp. 309–320, 2012.

[12] M. Manley, "Near-infrared spectroscopy and hyperspectral imaging: non-destructive analysis of biological materials," *Chemical Society Reviews*, vol. 43, no. 24, pp. 8200–8214, 2014.

[13] S. Mahesh, D. Jayas, J. Paliwal, and N. White, "Hyperspectral imaging to classify and monitor quality of agricultural materials," *Journal of Stored Products Research*, vol. 61, pp. 17–26, 2015.

[14] G. Bonifazi, G. Capobianco, and S. Serranti, "Asbestos containing materials detection and classification by the use of hyperspectral imaging," *Journal of hazardous materials*, vol. 344, pp. 981–993, 2018.

[15] O. Karpenko, A. Khomenko, E. Koricho, M. Haq, G. Cloud, and L. Udpa, "Monitoring of Impact Damage Accumulation in GFRP Composites Using Guided Waves and Optical Transmission Scanning," in *CAMX 2016 conference proceedings, CAMX the composites and advanced materials expo*, 2016.

[16] A. Khomenko, O. Karpenko, E. Koricho, M. Haq, G. L. Cloud, and L. Udpa, "Theory and validation of optical transmission scanning for quantitative NDE of impact damage in GFRP composites," *Composites Part B: Engineering*, vol. 107, pp. 182–191, 2016.

[17] A. Khomenko, O. Karpenko, E. G. Koricho, M. Haq, G. L. Cloud, and L. Udpa, "Quantitative comparison of optical transmission scanning with conventional techniques for NDE of impact damage in GFRP composites," *Composites Part B: Engineering*, vol. 123, pp. 92–104, 2017.

[18] B. Pan, K. Qian, H. Xie, and A. Asundi, "Two-dimensional digital image correlation for in-plane displacement and strain measurement: a review," *Measurement science and technology*, vol. 20, no. 6, p. 062001, 2009.

[19] K. Watanabe, I. Kobayashi, S. Saito, N. Kuroda, and S. Noshiro, "Nondestructive evaluation of drying stress level on wood surface using near-infrared spectroscopy," *Wood science and technology*, vol. 47, no. 2, pp. 299–315, 2013.

[20] N. Krumbholz, T. Hochrein, N. Vieweg, T. Hasek, K. Kretschmer, M. Bastian, M. Mikulics, and M. Koch, "Monitoring polymeric compounding processes inline with THz time-domain spectroscopy," *Polymer Testing*, vol. 28, no. 1, pp. 30–35, 2009.

[21] C. Jördens, M. Scheller, S. Wietzke, D. Romeike, C. Jansen, T. Zentgraf, K. Wiesauer, V. Reisecker, and M. Koch, "Terahertz spectroscopy to study the orientation of glass fibres in reinforced plastics," *Composites Science and Technology*, vol. 70, no. 3, pp. 472–477, 2010.

[22] C. Jansen, S. Wietzke, O. Peters, M. Scheller, N. Vieweg, M. Salhi, N. Krumbholz, C. Jördens, T. Hochrein, and M. Koch, "Terahertz imaging: Applications and perspectives," *Applied optics*, vol. 49, no. 19, pp. E48—-E57, 2010.

[23] I. Kang, M. J. Schulz, J. H. Kim, V. Shanov, and D. Shi, "A carbon nanotube strain sensor for structural health monitoring," *Smart materials and structures*, vol. 15, no. 3, p. 737, 2006.

[24] A. Raghavan, S. S. Kessler, C. T. Dunn, D. Barber, S. Wicks, and B. L. Wardle, "Structural health monitoring using carbon nanotube (CNT) enhanced composites," in *Proceedings of the 7th International Workshop on Structural Health Monitoring, Stanford University*, 2009.

[25] N. Alexopoulos, C. Bartholome, P. Poulin, and Z. Marioli-Riga, "Structural health monitoring of glass fiber reinforced composites using embedded carbon nanotube (CNT) fibers," *Composites Science and Technology*, vol. 70, no. 2, pp. 260–271, 2010.

[26] P. A. Withey, V. S. M. Vemuru, S. M. Bachilo, S. Nagarajaiah, and R. B. Weisman, "Strain paint: Noncontact strain measurement using single-walled carbon nanotube composite coatings," *Nano Letters*, vol. 12, no. 7, pp. 3497–3500, 2012.

[27] J. Sebastian, N. Schehl, M. Bouchard, M. Boehle, L. Li, A. Lagounov, and K. Lafdi, "Health monitoring of structural composites with embedded carbon nanotube coated glass fiber sensors," *Carbon*, vol. 66, pp. 191–200, 2014.

[28] M. Pimenta, A. Marucci, S. Empedocles, M. Bawendi, E. Hanlon, A. Rao, P. Eklund, R. Smalley, G. Dresselhaus, and M. Dresselhaus, "Raman modes of metallic carbon nanotubes," *Physical Review B*, vol. 58, no. 24, p. R16016, 1998.

[29] G. Gilliland, "Photoluminescence spectroscopy of crystalline semiconductors," *Materials Science and Engineering: R: Reports*, vol. 18, no. 3-6, pp. 99–399, 1997.

[30] S. Sugano and Y. Tanabe, "Absorption spectra of Cr^{3+} in Al_2O_3," *Journal of the Physical Society of Japan*, vol. 13, no. 8, pp. 880–899, 1958.

[31] H. Hough, J. Demas, T. Williams, and H. Wadley, "Luminescence sensing of stress in Ti/Al_2O_3 fiber reinforced composites," *Acta metallurgica et materialia*, vol. 43, no. 2, pp. 821–834, 1995.

[32] J. D. Barnett, S. Block, and G. J. Piermarini, "An optical fluorescence system for quantitative pressure measurement in the diamond-anvil cell," *Review of scientific instruments*, vol. 44, no. 1, pp. 1–9, 1973.

[33] R. J. Christensen, D. M. Lipkin, D. R. Clarke, and K. Murphy, "Nondestructive evaluation of the oxidation stresses through thermal barrier coatings using Cr^{3+} piezospectroscopy," *Applied Physics Letters*, vol. 69, no. 24, pp. 3754–3756, 1996.

[34] D. R. Clarke, M. Oechsner, and N. P. Padture, "Thermal-barrier coatings for more efficient gas-turbine engines," *MRS bulletin*, vol. 37, no. 10, pp. 891–898, 2012.

[35] B. Heeg and D. R. Clarke, "Non-destructive thermal barrier coating (TBC) damage assessment using laser-induced luminescence and infrared radiometry," *Surface and Coatings Technology*, vol. 200, no. 5-6, pp. 1298–1302, 2005.

[36] A. Manero II, A. Selimov, Q. Fouliard, K. Knipe, J. Wischek, C. Meid, A. M. Karlsson, M. Bartsch, and S. Raghavan, "Piezospectroscopic evaluation and damage identification for thermal barrier coatings subjected to simulated engine environments," *Surface and Coatings Technology*, vol. 323, pp. 30–38, 2017.

[37] S. Raghavan and P. K. Imbrie, "Ex-situ stress measurements in polycrystalline ceramics using photo-stimulated luminescence spectroscopy and high-energy x-rays," *Journal of the American Ceramic Society*, vol. 92, no. 7, pp. 1567–1573, 2009.

[38] L. Grabner, "Spectroscopic technique for the measurement of residual stress in sintered Al_2O_3," *Journal of Applied Physics*, vol. 49, no. 2, pp. 580–583, 1978.

[39] J. He and D. R. Clarke, "Determination of the piezospectroscopic coefficients for chromium-doped sapphire," *Journal of the American Ceramic Society*, vol. 78, no. 5, pp. 1347–1353, 1995.

[40] R. A. Forman, G. J. Piermarini, J. D. Barnett, and S. Block, "Pressure measurement made by the utilization of ruby sharp-line luminescence," *Science*, vol. 176, no. 4032, pp. 284–285, 1972.

[41] K. Hirsch and W. Holzapfel, "Diamond anvil high-pressure cell for Raman spectroscopy," *Review of Scientific Instruments*, vol. 52, no. 1, pp. 52–55, 1981.

[42] Y. H. Sohn, K. Schlichting, K. Vaidyanathan, M. Gell, and E. Jordan, "Nondestructive evaluation of residual stress for thermal barrier coated turbine blades by Cr^{3+} photoluminescence piezospectroscopy," *Metallurgical and Materials Transactions A*, vol. 31, no. 9, pp. 2388–2391, 2000.

[43] K. W. Schlichting, K. Vaidyanathan, Y. H. Sohn, E. H. Jordan, M. Gell, and N. P. Padture, "Application of Cr^{3+} photoluminescence piezo-spectroscopy to plasma-sprayed thermal barrier coatings for residual stress measurement," *Materials Science and Engineering: A*, vol. 291, no. 1-2, pp. 68–77, 2000.

[44] J. A. Nychka and D. R. Clarke, "Damage Quantification in TBCs by Photo-Stimulated Luminescence Spectroscopy," *Surface Coatings and Technology*, vol. 146-147, pp. 110–116, 2001. [Online]. Available: https://storage.cecs.ucf.edu//Groups/MMAE-Seetha/Literature/TBC/DamagequantificationinTBCsbyphotostimulatedluminescencespectroscopy.pdf

[45] A. Stevenson, A. Jones, and S. Raghavan, "Stress-sensing nanomaterial calibrated with photostimulated luminescence emission," *Nano Letters*, vol. 11, no. 8, pp. 3274–3278, 2011.

[46] ——, "Characterization of particle dispersion and volume fraction in alumina-filled epoxy nanocomposites using photo-stimulated luminescence spectroscopy," *Polymer journal*, vol. 43, no. 11, pp. 923–929, 2011.

[47] G. Freihofer, A. Schülzgen, and S. Raghavan, "Multiscale mechanics to determine nanocomposite elastic properties with piezospectroscopy," *Acta Materialia*, vol. 81, pp. 211–218, 2014.

[48] G. Freihofer, D. Fugon-Dessources, E. Ergin, A. Van Newkirk, A. Gupta, S. Seal, A. Schülzgen, and S. Raghavan, "Piezospectroscopic measurements capturing the evolution of plasma spray-coating stresses with substrate loads," *ACS applied materials & interfaces*, vol. 6, no. 3, pp. 1366–1369, 2014.

[49] G. Freihofer, A. Schulzgen, and S. Raghavan, "Damage mapping with a degrading elastic modulus using piezospectroscopic coatings," *NDT & E International*, vol. 75, pp. 65–71, 2015.

[50] G. Freihofer and S. Raghavan, "Characterization and Performance of Stress-and Damage-Sensing Smart Coatings," in *Industrial Applications for Intelligent Polymers and Coatings*. Springer, 2016, pp. 91–103.

[51] I. Hanhan, "Hybrid Carbon Fiber Alumina Nanocomposite for Non-Contact Stress Sensing Via Piezospectroscopy," 2015.

[52] A. Selimov, S. A. Jahan, E. Barker, P. Dackus, D. Carolan, A. Taylor, and S. Raghavan, "Silane functionalization effects on dispersion of alumina nanoparticles in hybrid carbon fiber composites," *Applied optics*, vol. 57, no. 23, pp. 6671–6678, 2018.

[53] S. A. Jahan, M. Abdelgader, E. Barker, J. Hernandez, R. Hoover, H. Pan, Y. Bai, D. Carolan, A. Taylor, and S. Raghavan, "Effect of functionalization on mechanical properties of hybrid carbon fiber reinforced polymer (HCFRP) composites using piezopectroscopy," in *2018 AIAA/ASCE/AHS/ASC Structures, Structural Dynamics, and Materials Conference*, 2018, p. 1378.

[54] *ASTM D695-15, Standard Test Method for Compressive Properties of Rigid Plastics*. West Conshohocken, PA: ASTM International, 2015. [Online]. Available: www.astm.org

[55] J. D. Eshelby, "The determination of the elastic field of an ellipsoidal inclusion, and related problems," *Proceedings of the royal society of London. Series A. Mathematical and physical sciences*, vol. 241, no. 1226, pp. 376–396, 1957.

[56] T. Mori and K. Tanaka, "Average stress in matrix and average elastic energy of materials with misfitting inclusions," *Acta metallurgica*, vol. 21, no. 5, pp. 571–574, 1973.

[57] M. Hussain, A. Nakahira, and K. Niihara, "Mechanical property improvement of carbon fiber reinforced epoxy composites by Al_2O_3 filler dispersion," *Materials Letters*, vol. 26, no. 3, pp. 185–191, 1996.

[58] A. Mohanty, V. K. Srivastava, and P. U. Sastry, "Investigation of mechanical properties of alumina nanoparticle-loaded hybrid glass/carbon-fiber-reinforced epoxy composites," *Journal of Applied Polymer Science*, vol. 131, no. 1, 2014.

[59] A. Alva and S. Raja, "Dynamic characteristics of epoxy hybrid nanocomposites," *Journal of reinforced plastics and composites*, vol. 30, no. 22, pp. 1857–1867, 2011.

[60] I. Hanhan, A. P. Selimov, D. Carolan, A. Taylor, and S. Raghavan, "Characterizing mechanical properties of hybrid alumina carbon fiber composites with piezospectroscopy," in *57th AIAA/ASCE/AHS/ASC Structures, Structural Dynamics, and Materials Conference*, 2016, p. 1413.

[61] A. Selimov, R. Hoover, Q. Fouliard, A. Manero II, P. Dackus, D. Carolan, A. Taylor, and S. Raghavan, "Characterization of Hybrid Carbon Fiber Composites using Photoluminescence Spectroscopy," in *58th AIAA/ASCE/AHS/ASC Structures, Structural Dynamics, and Materials Conference*, 2017, p. 123.

[62] J. Végh, "Alternative form for the pseudo-Voigt peak shape," *Review of scientific instruments*, vol. 76, no. 5, p. 056107, 2005.

[63] P. P. Camanho, P. Maimí, and C. Dávila, "Prediction of size effects in notched laminates using continuum damage mechanics," *Composites science and technology*, vol. 67, no. 13, pp. 2715–2727, 2007.

[64] *ASTM E8M-04, Standard Test Methods for Tension Testing of Metallic Materials (Metric)*. West Conshohocken, PA: ASTM International, 2004. [Online]. Available: www.astm.org

[65] R. Esteves, J. Hernandez, K. Vo, R. Hoover, G. Freihofer, and S. Raghavan, "Measurements for stress sensing of composites using tailored piezospectroscopic coatings," *AIP Advances*, vol. 9, no. 5, p. 55201, 2019.

[66] *ASTM D3039/D3039M-08, Standard Test Method for Tensile Properties of Polymer Matrix Composite Materials*. West Conshohocken, PA: ASTM International, 2008. [Online]. Available: www.astm.org

[67] *ASTM E647-00, Standard Test Method for Measurement of Fatigue Crack Growth Rates*. West Conshohocken, PA: ASTM International, 2000. [Online]. Available: www.astm.org

[68] *ASTM D5766/D5766M-11, Standard Test Method for Open-hole Tensile Strength of Polymer Matrix Composite Laminates*. West Conshohocken, PA: ASTM International, 2011. [Online]. Available: www.astm.org

[69] D. E. McCumber and M. D. Sturge, "Linewidth and Temperature Shift of the R Lines in Ruby," *Journal of Applied Physics*, vol. 34, no. 6, pp. 1682–1684, jan 1963. [Online]. Available: https://storage.cecs.ucf.edu//Groups/MMAE-Seetha/Literature/Piezospectroscopy/LinewidthandtemperatureshiftoftheRlinesofruby.pdf

[70] R. Munro, G. Piermarini, S. Block, and W. Holzapfel, "Model line-shape analysis for the ruby R lines used for pressure measurement," *Journal of Applied Physics*, vol. 57, no. 2, pp. 165–169, 1985.

[71] A. K. McBride, S. L. Turek, A. E. Zaghi, and K. A. Burke, "Mechanical behavior of hybrid glass/steel fiber reinforced epoxy composites," *Polymers*, vol. 9, no. 4, p. 151, 2017.

[72] M. Sabzi, S. Mirabedini, J. Zohuriaan-Mehr, and M. Atai, "Surface modification of TiO_2 nano-particles with silane coupling agent and investigation of its effect on the properties of polyurethane composite coating," *Progress in Organic Coatings*, vol. 65, no. 2, pp. 222–228, 2009.

[73] *Safety Data Sheet: EPON^{TM} Resin 828*, Hexion Inc. Std., Mar. 2016.

[74] *Safety Data Sheet: CA8000/B900A Base Component*, PPG Aerospace Std., Apr. 2018.

[75] I. Hanhan, E. Durnberg, G. Freihofer, P. Akin, and S. Raghavan, "Portable piezospectroscopy system: Non-contact in-situ stress sensing through high resolution photoluminescent mapping," *Journal of Instrumentation*, vol. 9, no. 11, 2014.

[76] E. Simova and P. A. Rochefort, "Active spectral imaging nondestructive evaluation (SINDE) camera," *CNL Nuclear Review*, vol. 5, no. 1, pp. 121–125, 2015.

[77] J. B. Abbiss and B. Heeg, "Imaging piezospectroscopy," *Review of Scientific Instruments*, vol. 79, no. 12, p. 123105, 2008.

[78] B. Heeg, J. B. Abbiss, A. I. Khizhnyak, and D. R. Clarke, "Spectral imaging device," Jun. 19 2008, uS Patent App. 11/957,244.